

COOL-LAMPS. VII. Quantifying Strong-lens Scaling Relations with 177 Cluster-scale Gravitational Lenses in DECaLS

SIMON D. MORK , MICHAEL D. GLADDERS , GOURAV KHULLAR , KEREN SHARON , NATHALIE CHICOINE ,
AIDAN P. CLOONAN , HÅKON DAHLE , DIEGO GARZA , ROWEN GLUSMAN , KATYA GOZMAN ,
GABRIELA HORWATH , BENJAMIN C. LEVINE , OLINA LIANG, DANIEL MAHRONIC, VIRAJ MANWADKAR ,
MICHAEL N. MARTINEZ , ALEXANDRA MASEGIAN , OWEN S. MATTHEWS ACUÑA , KAIYA MERZ , YUE PAN ,
JORGE A. SANCHEZ , ISAAC SIERRA , DANIEL J. KAVIN STEIN , EZRA SUKAY , MARCOS TAMARGO-ARIZMENDI ,
KIYAN TAVANGAR , RUOYANG TU , GRACE WAGNER , ERIK A. ZABOROWSKI  AND YUNCHONG ZHANG 

(COOL-LAMPS COLLABORATION)

Submitted to ApJ

ABSTRACT

We compute parametric measurements of the Einstein-radius-enclosed total mass for 177 cluster-scale strong gravitational lenses identified by the Chicago Optically-selected Lenses Located At the Margins of Public Surveys (COOL-LAMPS) collaboration with lens redshifts ranging from $0.2 \lesssim z \lesssim 1.0$ using only two measured parameters in each lensing system: the Einstein radius, and the brightest-cluster-galaxy (BCG) redshift. We then constrain the Einstein-radius-enclosed luminosity and stellar mass by fitting parametric spectral energy distributions (SEDs) with aperture photometry from the Dark Energy Camera Legacy Survey (DECaLS) in the g , r , and z -band Dark Energy Camera (DECam) filters. We find that the BCG redshift, enclosed total mass, and enclosed luminosity are strongly correlated and well described by a planar relationship in 3D space. We also find that the enclosed total mass and stellar mass are correlated with a logarithmic slope of 0.443 ± 0.035 , and the enclosed total mass and stellar-to-total mass fraction are correlated with a logarithmic slope of -0.563 ± 0.035 . The correlations described here can be used to validate strong-lensing candidates in upcoming imaging surveys—such as Rubin/Legacy Survey of Space and Time (LSST)—in which an algorithmic treatment of lensing systems will be needed due to the sheer volume of data these surveys will produce.

Keywords: Galaxy clusters (584) — High-redshift galaxy clusters (2007) — Scaling relations (2031) — Spectral energy distribution (2129) — Strong gravitational lensing (1643)

1. INTRODUCTION

Strong gravitational lensing is a rare phenomenon in the universe in which an intervening object with sufficient surface mass density bends light from a background source relative to the observer such that multiple images of the source are formed. For cases where the background source is a galaxy, the lensing effect can create highly distorted and magnified images of the source galaxy in an arclike shape (e.g., Lynds & Petrosian 1986;

Soucail et al. 1987; Kneib & Natarajan 2011; Meneghetti et al. 2013; Rivera-Thorsen et al. 2017; Shajib et al. 2022). The discovery of new gravitational lenses of this type is accelerating rapidly, particularly with the help of machine learning applied to finding galaxy-galaxy strong lenses in large optical-imaging surveys (e.g., Huang et al. 2021; Rojas et al. 2022; Zaborowski et al. 2023). Coupled with access to a flood of new data from large surveys such as Rubin/LSST in the coming years, the population of candidate lenses both in the bulk and at the margins will only grow. Contemporary methodologies often rely on visual inspection in order to winnow candidate lists to an acceptable number worthy of detailed follow-up (e.g.,

Diehl et al. 2017); such inspection has been successful in locating new systems thus far (e.g., Rojas et al. 2023). However, with thousands to millions of lines of sight to choose from in an ever-growing plethora of imaging data, statistical measures and correlations in existing lensing systems may help hone candidate-lens samples by quantifying instances of strong lensing in tandem with traditional morphological identification. This would produce a purer sample and help streamline the ability to identify targets. In this paper, we analyze a sample of 177 strong gravitational lenses identified via visual inspection by the COOL-LAMPS collaboration in DECaLS Legacy Survey Data Release 8 (LS DR8, Dey et al. 2019) images, and we investigate the scaling relations between the BCG redshift, Einstein-radius-enclosed (enclosed) total mass, enclosed luminosity, enclosed stellar mass, and enclosed stellar-to-total mass fraction therein. The sample we use here consists of a refined subsample of all strong-lensing candidates identified by COOL-LAMPS, and we consider them unambiguous and robust as informed by their visual morphology—despite a lack of definite spectroscopic confirmation.

Throughout this paper, we adopt a Λ CDM WMAP-9 cosmology (Hinshaw et al. 2013). All photometric calculations were done in the AB magnitude system.

2. METHODOLOGY

Galaxies and galaxy clusters host their mass in a variety of forms. Theory and observations both place strong constraints on observed stellar luminosity as a function of mass (e.g., Kuiper 1938; Presotto et al. 2014; Wang & Zhong 2018), hot intracluster gas contributes significantly to the total mass in galaxy clusters (e.g., Forman et al. 1972; Kellogg et al. 1972; Markevitch & Vikhlinin 2007), and both galaxies and galaxy clusters are composed of a significant fraction of dark matter (e.g., Zwicky 1933; Rubin 1986; Navarro et al. 1996; Bryan & Norman 1998; Hradecky et al. 2000). However, robustly measuring these mass components on a per-system basis is time and resource intensive—which is unsustainable for large samples. Conveniently, the existence of lensing prescribes a specific amount of mass that must exist to create the observed lensing *a priori*.

Remolina González et al. (2020) have shown that knowing only the angle between the BCG and lensed source arc (a proxy for Einstein radius; θ_E) and the line-of-sight geometry (redshift of the lens and the source; z_L, z_S), the core mass interior to the Einstein radius of a strong-lensing galaxy cluster may be measured with minimal scatter on order of $\approx 10\%$. With these three parameters, the mass can be immediately calculated and accounts for *all* of the projected mass density interior

to the Einstein radius. Measuring mass in this way also offers a well-defined aperture with which to constrain photometric properties of the lens as well. By directly integrating over pixels inside this aperture in flux-calibrated images, the lens-galaxy photometry can be automatically utilized by an SED modeller to obtain measurements of enclosed luminosity and stellar mass.

The COOL-LAMPS collaboration has constructed a large dataset of strong-lensing candidates using a simple human-led ranking system (e.g., Khullar et al. 2021; Sukay et al. 2022; Martinez et al. 2023; Zhang et al. 2023; Napier et al. 2023b; Klein et al. 2024). From this, we have collated a sample of 177 galaxy clusters and groups that exhibit robust visual evidence of strong gravitational lensing in which the primary lensed source arc is roughly circular with its projected center located at or very near to the BCG. Any systems with complex source-galaxy morphology are less likely to be well described by the simple symmetric dark-matter profiles that inform the parametric mass estimates described in Remolina González et al. (2020)—such complex systems were intentionally excluded from this work.

2.1. Einstein Radius

We defined the Einstein radius for each system as the radius of a circle centered on the BCG (Remolina González et al. 2020) which minimizes the total angular separation between each of the three most readily identifiable bright “clumps” in the tangentially lensed arcs and the perimeter of said circle. Henceforth, we refer to this circular aperture centered on the BCG with radius equal to the Einstein radius as the “Einstein aperture”. Four points (the BCG center and three points along each arc) physically constrain the Einstein aperture, and we obtained them by tagging the point of peak surface brightness for the BCG and similar peaks in surface brightness in the clumps of each tangentially lensed arc respectively. If three distinct peaks were unable to be found along the tangential arcs, the main arc was simply traced. We bootstrapped the three tangential-arc positional constraints 1000 times, and we adopted the mean and standard deviation from the resulting distribution of Einstein radii as the Einstein radius and its error respectively for each system. A descriptive visualization sampling the range of Einstein radii and lens redshifts considered in this work is shown in Figure 1.

2.2. Lens Redshift

BCGs are *sui generis* red-sequence cluster galaxies which can also be used as proxies to infer properties of the cluster-scale dark-matter halo (e.g., Oegerle & Hoesel 1991; Lauer et al. 2014). Since we assume that the

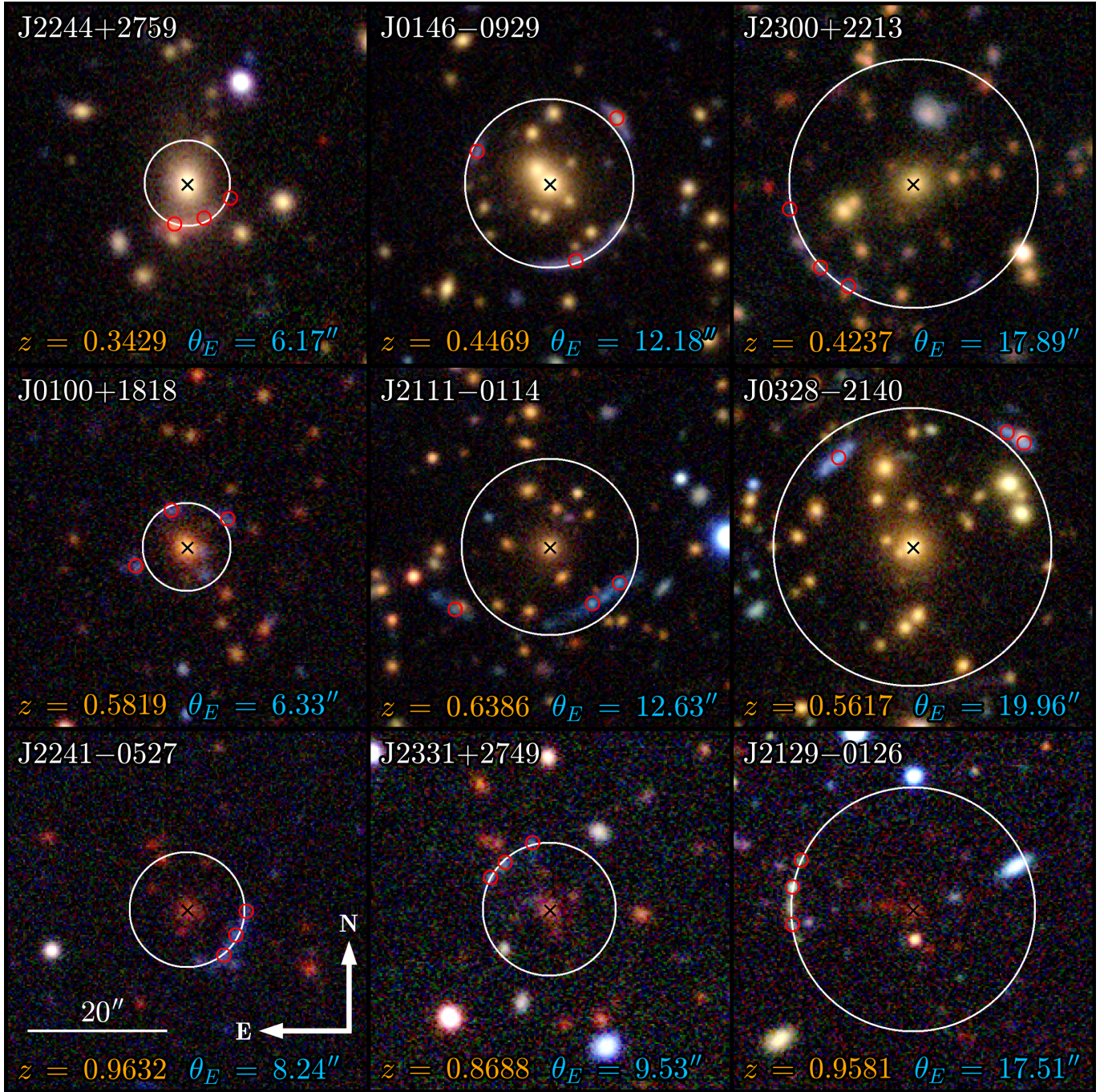


Figure 1. A subset of nine strong gravitational lenses analyzed in this work. The lenses are arranged by increasing redshift from the top to the bottom of the figure, and they are arranged by increasing Einstein radius from the left to the right of the figure. In each subplot, red circles denote positional constraints used to derive the Einstein radius, white circles represent the Einstein aperture, and a black ‘x’ marks the exact coordinates of the BCG. Respective lens redshifts and Einstein radii are also shown in each subplot. RGB images have equal astrometric scaling and are sourced from DECaLS LS DR9 (Dey et al. 2019) using z , r , and g -band imaging data with custom color scaling respectively.

lensing systems in this work can be well described by a symmetric dark-matter profile, we take the redshift of the BCG as interchangeable with the systematic redshift of the cluster-scale dark-matter halo. The lens redshift converts the measured Einstein radius to a proper trans-

verse distance via the angular diameter distance, and we queried the Sloan Digital Sky Survey Data Release 15 (SDSS DR15, Aguado et al. 2019; Kollmeier et al. 2019) in tandem with the Legacy Survey Data Release 9 (LS DR9, Dey et al. 2019; Duncan 2022) for each system in

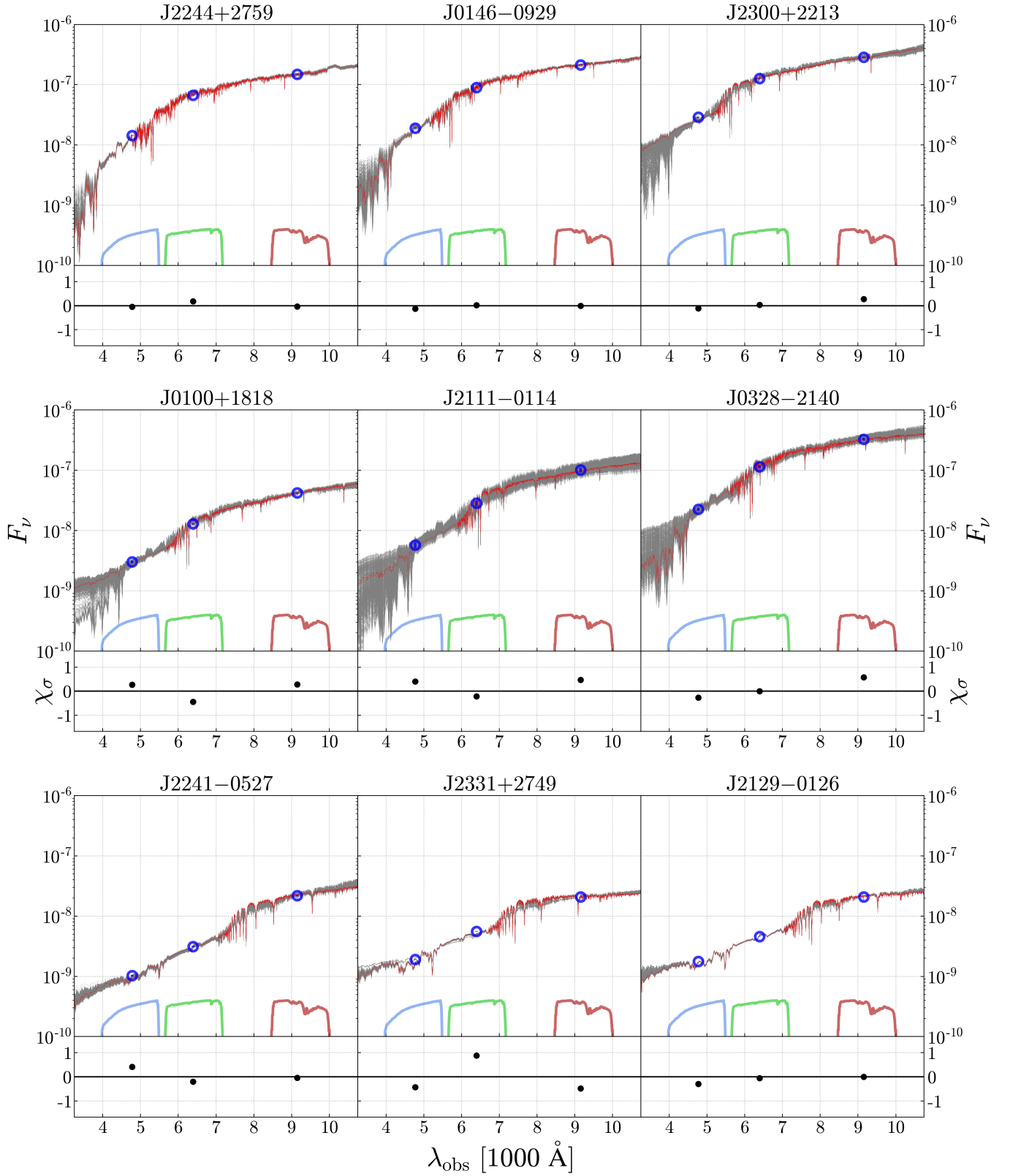


Figure 2. Observed-frame spectral energy distributions (SEDs) in maggies for the nine lenses shown in Figure 1 after SED fitting with *Prospector*. The top plot of each subplot contains the best-fit SED (red line), 1024 SEDs drawn from their respective posterior distributions (grey lines), observed lens-galaxy photometry (blue points), and photometric filter transmission curves for the Dark Energy Camera (DECam, [Flaugher et al. 2015](#)) *g*, *r*, and *z*-band filters from left to right respectively (in arbitrary units). The bottom plot of each subplot shows the residual between the observed photometry and the best-fit SED—normalized by the standard deviation of the observed photometry.

this work to obtain lens (BCG) redshifts. If the centroid coordinates for each BCG corresponded to a warning-free spectroscopic redshift in SDSS DR15, we adopted that redshift as the lens redshift for that system along with its associated error. If a given BCG lacked any corresponding value in SDSS DR15, as is the case for the higher redshift clusters in this work and/or clusters located in SDSS-non-imaged areas, we adopted the LS DR9 photometric redshift (Zhou et al. 2023) as the lens redshift and its associated error instead. We obtained spectroscopic redshifts for 41 systems and photometric redshifts for the remaining 136 systems.

2.3. Source Redshift

In strong lensing, the source redshift is typically constrained either with spectroscopic follow-up (e.g., Sharon et al. 2020) or by inferring a photometric redshift (e.g., Cerny et al. 2018). However, obtaining these redshifts for all identified source galaxies in a given system requires prolonged additional inquiry in tension with the appeal of an efficient mass estimator. Remolina González et al. (2020) have shown that substituting a single known source-galaxy redshift with a distribution of source-galaxy redshifts introduces a statistically insignificant uncertainty into the final distribution of mass measurements when compared to the magnitude of other systematic uncertainties. This distribution of lensed source redshifts is measurable (e.g., Bayliss et al. 2011a,b; Tran et al. 2022), and we simply adopt a well-described Gaussian with $\mu = 2$ and $\sigma = 0.2$ from Bayliss et al. (2011a) in keeping with the methodology of Remolina González et al. (2020) as the distribution of source redshifts across the entire sample in this work.

2.4. Photometry

We obtained aperture photometry for SED fitting in each system by linearly summing the dereddened flux from pixels within the Einstein aperture in g , r , and z -band imaging data from DECaLS LS DR9. Since it is critical that we do not include light from the lensed source arcs as well as any intervening stars or foreground galaxies in the measured photometry, we created two masks to exclude non-lens-galaxy regions. The first mask removed flux from the lensed source arcs, and the second mask removed flux from interlopers as identified by a color and magnitude screening by eye. Accounting for masking, this linear integration was done for each of the 1000 bootstrapped Einstein apertures derived in Section 2.1, and the resulting mean and standard deviation were adopted as the g , r , and z -band photometry and their errors respectively for each system.

3. ANALYSIS

3.1. Total Mass

Following Remolina González et al. (2020), the enclosed total mass within the Einstein aperture was calculated using Equations (1) and (2)—where $D(z)$ refers to the angular diameter distance at redshift z —via a Monte Carlo approach. The enclosed total mass was computed 1000 times for each system, in which each calculation used a different Einstein radius, source redshift, and lens redshift randomly drawn from a Gaussian distribution with mean equal to the parameter value and standard deviation equal to the parameter error. Also described in Remolina González et al. (2020) is the need to apply an empirical correction described in Equation (3) based on the “completeness” of the lensed source arcs in each system—where $f(\theta_E)$ is a cubic polynomial function specified in Table 1 of Remolina González et al. (2020). This is because the systematic bias and scatter of $M_\Sigma(< \theta_E)$ has a dependence on the degree of symmetry for each system, in which larger-Einstein-radius systems have a stronger offset. The correction factor aims to remove this dependence as a function of Einstein radius in non-perfectly symmetric systems.

$$\Sigma_{\text{cr}}(z_L, z_S) = \frac{c^2}{4\pi G} \frac{D_S(z_S)}{D_L(z_L)D_{LS}(z_L, z_S)} \quad (1)$$

$$M(< \theta_E) = \pi(D_L(z_L)\theta_E)^2 \Sigma_{\text{cr}}(z_L, z_S) \quad (2)$$

$$M_\Sigma(< \theta_E) = \frac{M(< \theta_E)}{f(\theta_E)} \quad (3)$$

For the purposes of applying this correction in each of the 177 lensing systems analyzed in this work, we measured the azimuthal coverage (ϕ)—defined as the percentage of the Einstein aperture that was traced out by the lensed source arcs in a given system. For example, a lens with a tangential arc stretching from an azimuthal angle of 10 to 100 degrees would have $\phi = 0.25$. As was done by Remolina González et al. (2020), ϕ was used as an observable proxy for the degree of symmetry in each system to determine whether or not the correction factor was needed. Larger-Einstein-radius systems with a predominantly low ϕ tend to deviate from a symmetric dark-matter halo and thus require the empirical correction. For spherically symmetric systems with a large ϕ , the measured $M_\Sigma(< \theta_E)$ is taken to be fairly unbiased, and thus the correction factor is not needed. We obtained ϕ by determining the fraction of the perimeter of the Einstein aperture that was subtended by the the regions masking the lensed source arcs described in Section 2.4 in each system. Adopting the convention used by Remolina González et al. (2020) in their analysis, if $\phi < 0.5$, Equation (3) was applied. If $\phi \geq 0.5$, it was

Table 1. Parameters used in SED Fitting with *Prospector*

Free	Parameter	Description	Priors
Y	$\log(M_{tot}/M_{\odot})$	Total stellar mass formed in dex solar masses.	Top Hat: [8.0, 14.0].
Y	$\log(Z/Z_{\odot})$	Stellar metallicity in dex solar metallicity.	Top Hat: [-1.0, 0.2].
Y	λ_2	Diffuse dust optical depth.	Top Hat: [0.0, 2.0].
Y	t_{age}	Age of the cluster in Gyr.	Top Hat: [$t_{z=20}$, $t_{z_{BCG}}$].
Y	τ	SFH e-folding time in Gyr.	Top Hat: [0.1, 10].
N	imf_type	Initial mass function type.	Chabrier (Chabrier 2003).
N	dust_type	Dust attenuation curve.	Calzetti (Calzetti et al. 2000).
N	sfh	Star formation history model.	Delayed tau (Carnall et al. 2019).

not applied. Accounting for the empirical correction, the mean and standard deviation of the 1000 measurements of $M_{\Sigma}(< \theta_E)$ were adopted as the enclosed total mass and its error respectively for each system.

3.2. Stellar Luminosity and Mass

We conducted parametric SED fitting using the photometry obtained in Section 2.4 with *Prospector* (Conroy et al. 2009; Conroy & Gunn 2010; Johnson et al. 2021, 2023); five free parameters and three assumed parameters parameterized each SED. A summary of all eight parameters used in fitting can be found in Table 1. Utilizing *emcee* (Foreman-Mackey et al. 2013) as implemented in *Prospector* with 84 walkers for a total of 6720 iterations, only the last 840 iterations for each of the 84 walkers (70,560 total parameter vectors) were taken as representing the posterior distribution for each of the five free parameters in each system in order to eliminate the significant burn-in sequence of the fitting process. After fitting, we adopted the 50th percentile of the posterior distribution as the value for each free parameter, and the greater difference between the 84th-50th percentile and 50th-16th percentile values as the error. Observed-frame SEDs for the systems shown in Figure 1 after SED fitting are shown in Figure 2.

To derive luminosity, we generated new SEDs with a random sample of 1024 free-parameter vectors from the posterior distributions of the best-fit SED in each system. We integrated over the rest-frame wavelength interval of 3000Å to 7000Å, since this corresponds to the longest wavelength interval sampled by part of at least two bands of photometry across all BCG redshifts in this work (the lower bound of 3000Å gets redshifted out of the g and into the r band at high redshifts). This range also allows us to sample the rest-frame 4000Å break while recovering flux in longer wavelengths which are significantly more luminous in cluster galaxies. After integrating the SEDs, we converted flux to luminosity

in solar luminosities using the appropriate luminosity distance and adopted the mean and standard deviation from the 1024 random parameter vectors as the luminosity and its error respectively for each system.

4. RESULTS

As Figure 3 shows, the BCG redshift, enclosed total mass, and enclosed luminosity are correlated. Indeed, we note that the most massive clusters in this work also possess a large stellar mass and thus have a large luminosity. Using *emcee*, we constrained a plane-of-best-fit using a likelihood maximization estimation taking into account the error in data on all three axes to describe this correlation—where $X = z_{BCG}$, $Y = \log_{10}[M_{\Sigma}(< \theta_E)/M_{\odot}]$, and $Z = \log_{10}[L(< \theta_E)/L_{\odot}]$ —yielding:

$$Z = 0.137^{+0.051}_{-0.051}X + 0.522^{+0.022}_{-0.023}Y + 4.207^{+0.300}_{-0.290} \quad (4)$$

This simple and analytic relationship derived from a sample of known strong lenses, considering only quantities derived from observations, may have utility in differentiating *bona fide* strong lenses from non-lenses in large samples of candidate lenses where the evidence of lensing is not nearly as robust as the sample of clusters analyzed here. Moreover, this correlation offers a future opportunity to test simulations against observations—particularly those that aim to generate realistic galaxy populations in dense cluster environments.

A full accounting of all measured quantities in this work can be found in Table 2.

5. DISCUSSION

5.1. Scaling Relations

Besides the enclosed total mass and luminosity, we can also infer the observed enclosed stellar mass at the redshift of observation for each system using the stellar-mass posterior distribution from each SED constrained

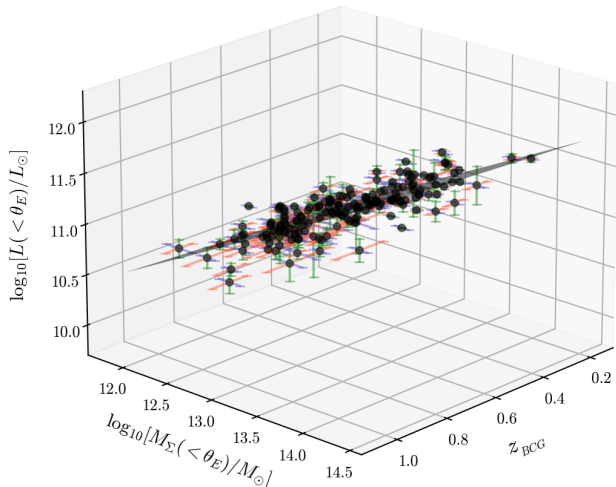


Figure 3. A 3D visualization of the BCG redshift, enclosed total mass, and enclosed luminosity for the systems in this work plotted as black circles. A plane-of-best-fit is also shown in black as well. Errors in data on each axis are represented as red, blue, and green lines respectively.

with *Prospector*. We obtained this by correcting the derived enclosed stellar mass formed in each system with the surviving mass fraction returned by *Prospector*. This is necessary because the amount of stellar mass that we see at the redshift of observation is less than the total stellar mass formed over the lifetime of the galaxy (e.g., Li et al. 2017)—the latter being what *Prospector* parametrically fits. While we note that enclosed stellar mass is more complex to infer and subject to more significant systematics when compared to the more direct measures of enclosed total mass from strong-lensing geometry and luminosity, it nevertheless offers another point of comparison with those measurables.

5.1.1. Total Mass — Stellar Mass

In Panel I of Figure 4, we see a clearly positive correlation between the enclosed total mass and the enclosed stellar mass for all systems. By performing a linear regression with *emcee* using a likelihood maximization estimation that accounts for errors in data on both axes, we find that the slope of this correlation is 0.443 ± 0.035 from the posterior distribution of the MCMC fit. We colored the points according to their luminosity to highlight how the intrinsic differences between individual systems contribute to the overall intrinsic scatter. In Table 2 of Kravtsov et al. (2018), they found M_{500} (White 2001) and the stellar mass of solely the BCG to be correlated with a logarithmic slope of 0.33 ± 0.11 . In addition, Kravtsov et al. (2018) found M_{500} and the stellar mass of the entire cluster to be correlated with a logarithmic slope of 0.59 ± 0.08 . The fact that the slope for this work

falls between the two slopes quoted by Kravtsov et al. (2018) is consistent with how our methodology samples a physical regime between exclusively the BCG and that of the entire cluster.

Panel II of Figure 4 further explores this correlation, with only those clusters where multiple cluster members were contained within the Einstein aperture are plotted. A linear regression for the multiple-galaxy systems gives a slope of 0.453 ± 0.049 , which is consistent with the slope using all systems.

5.1.2. Total Mass — Stellar-to-Total Mass Fraction

In Panel III of Figure 4, we plot the enclosed stellar-to-total mass fraction against the enclosed total mass and see a clearly negative correlation (again with the same colormapping as Panel I to emphasize intrinsic scatter). Also using *emcee*, we find that the slope of this correlation is -0.563 ± 0.035 . Categorizing in Panel IV identically to Panel II, we find that the multiple-galaxy systems are correlated with a slope of -0.561 ± 0.050 . We again find that the slope for the multiple-galaxy systems are statistically indistinguishable from the slope for the entire sample shown in Panel III. Andreon (2010) measured 52 clusters over a slightly larger mass range and found that the stellar mass fraction depended on halo mass with a slope of -0.55 ± 0.08 when measuring out to a physical extent of R_{200} . Both of the slopes in Panels III and IV are statistically similar to Andreon (2010), and while the linear fit derived by Andreon (2010) has a slightly larger normalization, this is to be expected because the cluster masses are constrained out to R_{200} .

5.2. Photometric Bias and Error

Deriving light in Section 2.4 via directly integrating over the Einstein aperture presents some challenges. Since we identified red-sequence cluster members by using observed color as a proxy for cluster membership, it is possible that we may have included intrinsically bluer galaxies at redshift $z > z_{BCG}$ that appear to be the same color as the cluster members. Conversely, we may have excluded intrinsically bluer *bona fide* cluster members. However, star-forming cluster members have less stellar mass and are intrinsically rarer in cluster cores (e.g., Dressler et al. 1997, 2004), and we do not expect that these missed cluster galaxies introduce a significant loss to the measured cluster light. In addition, bluer galaxies at redshift $z > z_{BCG}$ appear relatively fainter, which are also unlikely to bias our methodology of measuring cluster light. Interlopers such as foreground stars that appear in front of cluster galaxies are forced to be masked, but any underlying lens-galaxy flux is typically minimal due to the limited angular size of such stars.

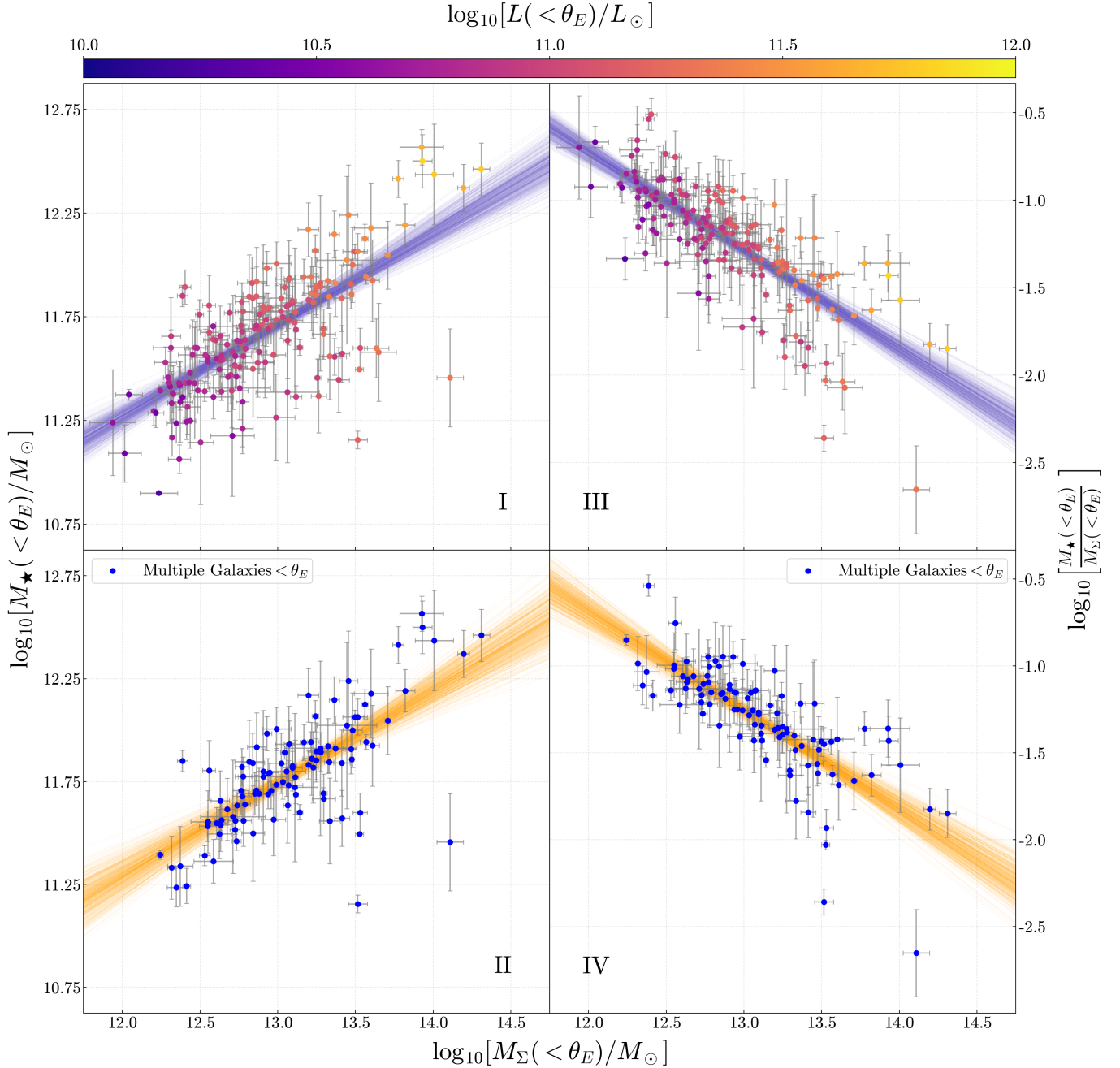


Figure 4. The total mass enclosed within the Einstein aperture for each system on the x-axis plotted against both the enclosed stellar mass and the enclosed stellar-to-total mass fraction on the y-axes. Points in Panels I and III are color coded according to the luminosity of the system in units of solar luminosities from stellar light enclosed within the Einstein aperture as measured within the rest-frame wavelength interval of 3000Å to 7000Å. Points in Panels II and IV only represent systems in which multiple cluster members fall within the Einstein aperture. Linear regression lines in all four Panels are drawn from the posterior distributions of their respective MCMC.

In general, we expect that all of the unmasked flux from cluster cores at the angular scales considered in this work originates from genuine cluster members. Any modest background correction that could be made will also be effectively captured in the redshift dependence of the fits (e.g., Figure 3). While we must also con-

sider associated galaxy populations in the immediate large-scale structure when considering galaxy clusters projected onto the sky—as such structures may also be projected onto the cluster core—those galaxies will also contribute to the lensing effect and will have their mass and light captured by the methodology presented here.

We also note that our sample contains extremely few examples of systems which have a measured Einstein radius of $\theta_E \lesssim 2''$. To some extent, this is a consequence of our chosen sample of cluster-scale lenses, which we would generally expect to have larger Einstein radii. However, we caution that there exists a large scatter between the total halo mass and Einstein radius (Fox et al. 2022). Systems whose arcs are separated from the central galaxy at small radii may also be located directly within the discernable BCG light. This would not only make them hard to visually notice, but it would also make them unsuitable for this analysis because the source light would be significantly blended together with the lensing cluster light. While we thus expect this work to undersample the small-Einstein-radius regime, it is not apparent that this significantly alters our findings.

In addition, our use of relatively shallow ground-based imaging limits the 5σ point-source magnitude depth of objects in the g , r , and z -band filters to ≈ 24.7 , 23.9 , and 23.0 respectively in the average case of two exposures per filter (Dey et al. 2019). Systems with a lens redshift $z \gtrsim 1$ are barely visible even in z -band LS DR9 imaging data, and they are also simply a rarer type of lensing system in the universe (Li et al. 2019). Both the data depth and intrinsic redshift distribution of lenses shape the redshift distribution in this work.

5.3. Alternative Mass Measurement

In constraining mass, we also considered a second method for measuring cluster-centric mass elucidated in Remolina González et al. (2021a) using the parametric lens-modelling software LENSTOOL (Jullo et al. 2007) to measure the enclosed total mass—as opposed to the simple evaluation of Equations (1), (2), and (3). For the first 35 clusters that were analyzed in this work, we generated single-halo lens models by taking the three coordinates in each lensed arc used to derive the Einstein radius in Section 2.1 as a multiple-image family with a single pseudo-isothermal elliptical mass distribution (PIEMD, Kassiola & Kovner 1993) locked to the center of the BCG. Mass estimates were then obtained from the resulting best-fit lens models according to the methodology described in Remolina González et al. (2021a).

As expected from Remolina González et al. (2021b), these differing methodologies show similar results. The two mass measurements for the 35 clusters studied here are correlated with a slope of 0.960 ± 0.036 and intercept of 0.492 ± 0.476 dex as shown in Figure 5. In other words, we find no reason to suggest a preference between one method over the other, and we abandoned the LENSTOOL approach in favor of the much faster parametric approach throughout the rest of the work.

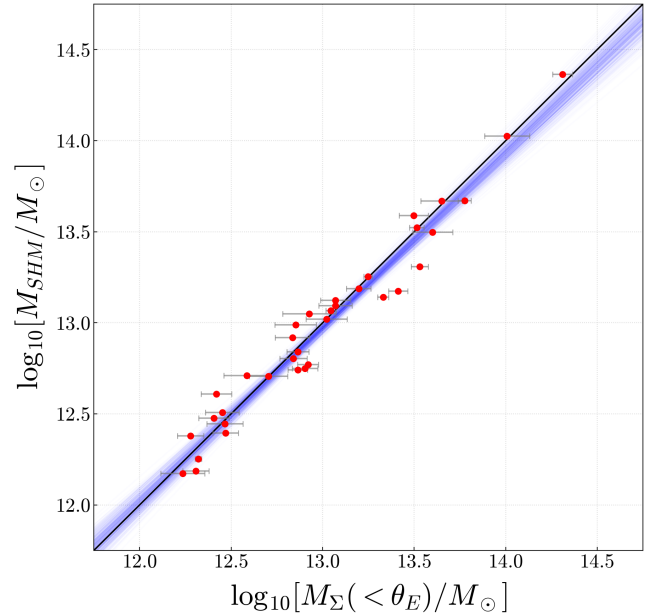


Figure 5. A comparison of the single-halo LENSTOOL-generated mass measurements (M_{SHM}) and the parametrically generated mass measurements (M_{Σ}) for the first 35 clusters analyzed in this work. The black line represents an ideal 1-1 correspondence, and the blue lines represent the uncertainty on the measured correspondence.

In theory, lens modelling has the potential to be the most accurate mass-constraining methodology. However, this requires high-spatial-resolution imaging data and ample time. The process of iteratively refining just one lens model may take upwards of an hour for even a single relatively simple system—which is untenable when the number of candidate systems reaches into the thousands. Moreover, the accuracy of measuring mass with lens modelling is sensitive to the choice of defining multiple-image families along the lensed source arcs in a way that simple circle fitting is not. These essential positional constraints are often unresolved even with the highest-quality ground-based imaging data. Conversely, the positional constraints that inform the Einstein radius ultimately used by Equations (1), (2), and (3) need not be extremely accurate with respect to exactly constraining image family positions. As long as the positional constraints are reasonably placed within the arcs, something which *is* resolved by ground-based imaging data, it is accurate to within the systematic uncertainty.

For more information on lens-modelling software, related techniques, and applications of strong lensing, we refer the reader to the following non-exhaustive list of papers for further review: Elíasdóttir et al. (2007), Oguri (2010), Lefor et al. (2013), Meneghetti et al. (2017), Birrer & Amara (2018), Schäfer et al. (2020), Sharon et al. (2022), and Napier et al. (2023a).

6. SUMMARY AND CONCLUSIONS

This paper presents measurements of mass and light in 177 strong-lensing systems at cluster and group mass scales. By directly obtaining the Einstein radius and BCG redshift for each system, we compute the Einstein-radius-enclosed total mass parametrically. We use the enclosed g , r , and z -band photometry with **Prospector** to parameterize the enclosed luminosity and stellar mass, and we obtain a planar relationship between the BCG redshift, enclosed total mass, and enclosed luminosity of the form $Z = 0.137_{-0.051}^{+0.051}X + 0.522_{-0.023}^{+0.022}Y + 4.207_{-0.290}^{+0.300}$ where $X = z_{BCG}$, $Y = \log_{10}[M_{\Sigma}(< \theta_E)/M_{\odot}]$, and $Z = \log_{10}[L(< \theta_E)/L_{\odot}]$. We find that the enclosed total mass and stellar mass for the entire sample of strong-lensing systems considered in this work are correlated with a logarithmic slope, normalization, and intrinsic stellar-mass scatter of 0.443 ± 0.035 , 5.958 ± 0.454 dex, and 0.173 ± 0.013 dex respectively. We also find that the enclosed total mass and stellar-to-total mass fraction are correlated with a logarithmic slope, normalization, and intrinsic stellar-to-total-mass-fraction scatter of -0.563 ± 0.035 , 6.034 ± 0.457 dex, and 0.161 ± 0.013 dex respectively. Enormous volumes of imaging data from new space-based and ground-based surveys at deeper and sharper photometric limits are on the horizon. Probing these upcoming datasets with both visual and machine-learning driven searches for new strong lenses at a variety of scales is inevitable. The correlations shown in this work should have utility in filtering rankings of possible strong-lensing systems as well as offering another measure of cluster cores that can be compared to cosmological simulations.

ACKNOWLEDGMENTS

This work is supported by The College undergraduate program and the College Innovation Fund at the University of Chicago and the Department of Astronomy and Astrophysics at the University of Chicago.

The Legacy Surveys consist of three individual and complementary projects: the Dark Energy Camera Legacy Survey (DECaLS; Proposal ID #2014B-0404; PIs: David Schlegel and Arjun Dey), the Beijing-Arizona Sky Survey (BASS; NOAO Prop. ID #2015A-0801; PIs: Zhou Xu and Xiaohui Fan), and the Mayall z -band Legacy Survey (MzLS; Prop. ID #2016A-0453; PI: Arjun Dey). DECaLS, BASS and MzLS together include data obtained, respectively, at the Blanco telescope, Cerro Tololo Inter-American Observatory, NSF’s NOIRLab; the Bok telescope, Steward Observatory, University of Arizona; and the Mayall telescope, Kitt Peak National Observatory, NOIRLab. Pipeline processing and analyses of the data were supported by

NOIRLab and the Lawrence Berkeley National Laboratory (LBNL). The Legacy Surveys project is honored to be permitted to conduct astronomical research on Iolkam Du’ag (Kitt Peak), a mountain with particular significance to the Tohono O’odham Nation.

NOIRLab is operated by the Association of Universities for Research in Astronomy (AURA) under a cooperative agreement with the National Science Foundation. LBNL is managed by the Regents of the University of California under contract to the U.S. Department of Energy.

This project used data obtained with the Dark Energy Camera (DECam), which was constructed by the Dark Energy Survey (DES) collaboration. Funding for the DES Projects has been provided by the U.S. Department of Energy, the U.S. National Science Foundation, the Ministry of Science and Education of Spain, the Science and Technology Facilities Council of the United Kingdom, the Higher Education Funding Council for England, the National Center for Supercomputing Applications at the University of Illinois at Urbana-Champaign, the Kavli Institute of Cosmological Physics at the University of Chicago, Center for Cosmology and Astro-Particle Physics at the Ohio State University, the Mitchell Institute for Fundamental Physics and Astronomy at Texas A&M University, Financiadora de Estudos e Projetos, Fundacao Carlos Chagas Filho de Amparo, Financiadora de Estudos e Projetos, Fundacao Carlos Chagas Filho de Amparo a Pesquisa do Estado do Rio de Janeiro, Conselho Nacional de Desenvolvimento Cientifico e Tecnologico and the Ministerio da Ciencia, Tecnologia e Inovacao, the Deutsche Forschungsgemeinschaft and the Collaborating Institutions in the Dark Energy Survey. The Collaborating Institutions are Argonne National Laboratory, the University of California at Santa Cruz, the University of Cambridge, Centro de Investigaciones Energeticas, Medioambientales y Tecnologicas-Madrid, the University of Chicago, University College London, the DES-Brazil Consortium, the University of Edinburgh, the Eidgenossische Technische Hochschule (ETH) Zurich, Fermi National Accelerator Laboratory, the University of Illinois at Urbana-Champaign, the Institut de Ciencies de l’Espai (IEEC/CSIC), the Institut de Fisica d’Altes Energies, Lawrence Berkeley National Laboratory, the Ludwig Maximilians Universitat Munchen and the associated Excellence Cluster Universe, the University of Michigan, NSF’s NOIRLab, the University of Nottingham, the Ohio State University, the University of Pennsylvania, the University of Portsmouth, SLAC National Accelerator Laboratory, Stanford University, the University of Sussex, and Texas A&M University.

BASS is a key project of the Telescope Access Program (TAP), which has been funded by the National Astronomical Observatories of China, the Chinese Academy of Sciences (the Strategic Priority Research Program “The Emergence of Cosmological Structures” Grant # XDB09000000), and the Special Fund for Astronomy from the Ministry of Finance. The BASS is also supported by the External Cooperation Program of Chinese Academy of Sciences (Grant # 114A11KYSB20160057), and Chinese National Natural Science Foundation (Grant # 12120101003, # 11433005).

The Legacy Survey team makes use of data products from the Near-Earth Object Wide-field Infrared Survey Explorer (NEOWISE), which is a project of the Jet Propulsion Laboratory/California Institute of Technology. NEOWISE is funded by the National Aeronautics and Space Administration.

The Legacy Surveys imaging of the DESI footprint is supported by the Director, Office of Science, Office of High Energy Physics of the U.S. Department of Energy under Contract No. DE-AC02-05CH1123, by the National Energy Research Scientific Computing Center, a DOE Office of Science User Facility under the same contract; and by the U.S. National Science Foundation, Division of Astronomical Sciences under Contract No. AST-0950945 to NOAO.

The Photometric Redshifts for the Legacy Surveys (PRLS) catalog used in this paper was produced thanks to funding from the U.S. Department of Energy Office of Science, Office of High Energy Physics via grant DE-SC0007914.

Funding for the Sloan Digital Sky Survey V has been provided by the Alfred P. Sloan Foundation, the Heising-Simons Foundation, the National Science Foundation, and the Participating Institutions. SDSS ac-

knowledges support and resources from the Center for High-Performance Computing at the University of Utah. The SDSS web site is www.sdss.org.

SDSS is managed by the Astrophysical Research Consortium for the Participating Institutions of the SDSS Collaboration, including the Carnegie Institution for Science, Chilean National Time Allocation Committee (CNTAC) ratified researchers, the Gotham Participation Group, Harvard University, Heidelberg University, The Johns Hopkins University, L’Ecole polytechnique fédérale de Lausanne (EPFL), Leibniz-Institut für Astrophysik Potsdam (AIP), Max-Planck-Institut für Astronomie (MPIA Heidelberg), Max-Planck-Institut für Extraterrestrische Physik (MPE), Nanjing University, National Astronomical Observatories of China (NAOC), New Mexico State University, The Ohio State University, Pennsylvania State University, Smithsonian Astrophysical Observatory, Space Telescope Science Institute (STScI), the Stellar Astrophysics Participation Group, Universidad Nacional Autónoma de México, University of Arizona, University of Colorado Boulder, University of Illinois at Urbana-Champaign, University of Toronto, University of Utah, University of Virginia, Yale University, and Yunnan University.

Facilities: APO/2.5m SDSS Telescope, CTIO/4m Blanco Telescope.

Software: `astropy` (Astropy Collaboration et al. 2013, 2018, 2022), `astro-prospector` (Johnson et al. 2021), `emcee` (Foreman-Mackey et al. 2013), `FSPS` (Conroy et al. 2009; Conroy & Gunn 2010) `Jupyter Notebook` (Kluyver et al. 2016), `LENSTOOL` (Jullo et al. 2007), `matplotlib` (Hunter 2007), `numpy` (Harris et al. 2020), `pandas` (Wes McKinney 2010), `python-FSPS` (Johnson et al. 2023), `SAOImageDS9` (Joye & Mandel 2003), `scipy` (Virtanen et al. 2020).

REFERENCES

- Aguado, D. S., Ahumada, R., Almeida, A., et al. 2019, *ApJS*, 240, 23, doi: [10.3847/1538-4365/aaf651](https://doi.org/10.3847/1538-4365/aaf651)
- Andreon, S. 2010, *MNRAS*, 407, 263, doi: [10.1111/j.1365-2966.2010.16856.x](https://doi.org/10.1111/j.1365-2966.2010.16856.x)
- Astropy Collaboration, Robitaille, T. P., Tollerud, E. J., et al. 2013, *A&A*, 558, A33, doi: [10.1051/0004-6361/201322068](https://doi.org/10.1051/0004-6361/201322068)
- Astropy Collaboration, Price-Whelan, A. M., Sipőcz, B. M., et al. 2018, *AJ*, 156, 123, doi: [10.3847/1538-3881/aabc4f](https://doi.org/10.3847/1538-3881/aabc4f)
- Astropy Collaboration, Price-Whelan, A. M., Lim, P. L., et al. 2022, *ApJ*, 935, 167, doi: [10.3847/1538-4357/ac7c74](https://doi.org/10.3847/1538-4357/ac7c74)
- Bayliss, M. B., Gladders, M. D., Oguri, M., et al. 2011a, *ApJL*, 727, L26, doi: [10.1088/2041-8205/727/1/L26](https://doi.org/10.1088/2041-8205/727/1/L26)
- Bayliss, M. B., Hennawi, J. F., Gladders, M. D., et al. 2011b, *ApJS*, 193, 8, doi: [10.1088/0067-0049/193/1/8](https://doi.org/10.1088/0067-0049/193/1/8)
- Birrer, S., & Amara, A. 2018, *Physics of the Dark Universe*, 22, 189, doi: [10.1016/j.dark.2018.11.002](https://doi.org/10.1016/j.dark.2018.11.002)
- Bryan, G. L., & Norman, M. L. 1998, *ApJ*, 495, 80, doi: [10.1086/305262](https://doi.org/10.1086/305262)
- Calzetti, D., Armus, L., Bohlin, R. C., et al. 2000, *ApJ*, 533, 682, doi: [10.1086/308692](https://doi.org/10.1086/308692)
- Carnall, A. C., Leja, J., Johnson, B. D., et al. 2019, *ApJ*, 873, 44, doi: [10.3847/1538-4357/ab04a2](https://doi.org/10.3847/1538-4357/ab04a2)
- Cerny, C., Sharon, K., Andrade-Santos, F., et al. 2018, *ApJ*, 859, 159, doi: [10.3847/1538-4357/aabe7b](https://doi.org/10.3847/1538-4357/aabe7b)
- Chabrier, G. 2003, *PASP*, 115, 763, doi: [10.1086/376392](https://doi.org/10.1086/376392)

- Conroy, C., & Gunn, J. E. 2010, *ApJ*, 712, 833, doi: [10.1088/0004-637X/712/2/833](https://doi.org/10.1088/0004-637X/712/2/833)
- Conroy, C., Gunn, J. E., & White, M. 2009, *ApJ*, 699, 486, doi: [10.1088/0004-637X/699/1/486](https://doi.org/10.1088/0004-637X/699/1/486)
- Dey, A., Schlegel, D. J., Lang, D., et al. 2019, *AJ*, 157, 168, doi: [10.3847/1538-3881/ab089d](https://doi.org/10.3847/1538-3881/ab089d)
- Diehl, H. T., Buckley-Geer, E. J., Lindgren, K. A., et al. 2017, *ApJS*, 232, 15, doi: [10.3847/1538-4365/aa8667](https://doi.org/10.3847/1538-4365/aa8667)
- Dressler, A., Oemler, Augustus, J., Poggianti, B. M., et al. 2004, *ApJ*, 617, 867, doi: [10.1086/424890](https://doi.org/10.1086/424890)
- Dressler, A., Oemler, Augustus, J., Couch, W. J., et al. 1997, *ApJ*, 490, 577, doi: [10.1086/304890](https://doi.org/10.1086/304890)
- Duncan, K. J. 2022, *MNRAS*, 512, 3662, doi: [10.1093/mnras/stac608](https://doi.org/10.1093/mnras/stac608)
- Elíasdóttir, Á., Limousin, M., Richard, J., et al. 2007, arXiv e-prints, arXiv:0710.5636, doi: [10.48550/arXiv.0710.5636](https://doi.org/10.48550/arXiv.0710.5636)
- Flaugher, B., Diehl, H. T., Honscheid, K., et al. 2015, *AJ*, 150, 150, doi: [10.1088/0004-6256/150/5/150](https://doi.org/10.1088/0004-6256/150/5/150)
- Foreman-Mackey, D., Hogg, D. W., Lang, D., & Goodman, J. 2013, *PASP*, 125, 306, doi: [10.1086/670067](https://doi.org/10.1086/670067)
- Forman, W., Kellogg, E., Gursky, H., Tananbaum, H., & Giacconi, R. 1972, *ApJ*, 178, 309, doi: [10.1086/151791](https://doi.org/10.1086/151791)
- Fox, C., Mahler, G., Sharon, K., & Remolina González, J. D. 2022, *ApJ*, 928, 87, doi: [10.3847/1538-4357/ac5024](https://doi.org/10.3847/1538-4357/ac5024)
- Harris, C. R., Millman, K. J., van der Walt, S. J., et al. 2020, *Nature*, 585, 357, doi: [10.1038/s41586-020-2649-2](https://doi.org/10.1038/s41586-020-2649-2)
- Hinshaw, G., Larson, D., Komatsu, E., et al. 2013, *ApJS*, 208, 19, doi: [10.1088/0067-0049/208/2/19](https://doi.org/10.1088/0067-0049/208/2/19)
- Hradecky, V., Jones, C., Donnelly, R. H., et al. 2000, *ApJ*, 543, 521, doi: [10.1086/317158](https://doi.org/10.1086/317158)
- Huang, X., Storfer, C., Gu, A., et al. 2021, *ApJ*, 909, 27, doi: [10.3847/1538-4357/abd62b](https://doi.org/10.3847/1538-4357/abd62b)
- Hunter, J. D. 2007, *Computing in Science & Engineering*, 9, 90, doi: [10.1109/MCSE.2007.55](https://doi.org/10.1109/MCSE.2007.55)
- Johnson, B., Foreman-Mackey, D., Sick, J., et al. 2023, *dfm/python-fsps: v0.4.6, v0.4.6*, Zenodo, doi: [10.5281/zenodo.10026684](https://doi.org/10.5281/zenodo.10026684)
- Johnson, B. D., Leja, J., Conroy, C., & Speagle, J. S. 2021, *ApJS*, 254, 22, doi: [10.3847/1538-4365/abef67](https://doi.org/10.3847/1538-4365/abef67)
- Joye, W. A., & Mandel, E. 2003, in *Astronomical Society of the Pacific Conference Series*, Vol. 295, *Astronomical Data Analysis Software and Systems XII*, ed. H. E. Payne, R. I. Jedrzejewski, & R. N. Hook, 489
- Jullo, E., Kneib, J. P., Limousin, M., et al. 2007, *New Journal of Physics*, 9, 447, doi: [10.1088/1367-2630/9/12/447](https://doi.org/10.1088/1367-2630/9/12/447)
- Kassiola, A., & Kovner, I. 1993, *ApJ*, 417, 450, doi: [10.1086/173325](https://doi.org/10.1086/173325)
- Kellogg, E., Gursky, H., Tananbaum, H., Giacconi, R., & Pounds, K. 1972, *ApJL*, 174, L65, doi: [10.1086/180950](https://doi.org/10.1086/180950)
- Khullar, G., Gozman, K., Lin, J. J., et al. 2021, *ApJ*, 906, 107, doi: [10.3847/1538-4357/abcb86](https://doi.org/10.3847/1538-4357/abcb86)
- Klein, M., Sharon, K., Napier, K., et al. 2024, *COOL-LAMPS VI: Lens model and New Constraints on the Properties of COOL J1241+2219, a Bright z = 5 Lyman Break Galaxy and its z = 1 Cluster Lens*. <https://arxiv.org/abs/2401.10168>
- Kluyver, T., Ragan-Kelley, B., Pérez, F., et al. 2016, in *Positioning and Power in Academic Publishing: Players, Agents and Agendas*, ed. F. Loizides & B. Schmidt, IOS Press, 87 – 90
- Kneib, J.-P., & Natarajan, P. 2011, *A&A Rv*, 19, 47, doi: [10.1007/s00159-011-0047-3](https://doi.org/10.1007/s00159-011-0047-3)
- Kollmeier, J., Anderson, S. F., Blanc, G. A., et al. 2019, in *Bulletin of the American Astronomical Society*, Vol. 51, 274
- Kravtsov, A. V., Vikhlinin, A. A., & Meshcheryakov, A. V. 2018, *Astronomy Letters*, 44, 8, doi: [10.1134/S1063773717120015](https://doi.org/10.1134/S1063773717120015)
- Kuiper, G. P. 1938, *ApJ*, 88, 472, doi: [10.1086/143999](https://doi.org/10.1086/143999)
- Lauer, T. R., Postman, M., Strauss, M. A., Graves, G. J., & Chisari, N. E. 2014, *ApJ*, 797, 82, doi: [10.1088/0004-637X/797/2/82](https://doi.org/10.1088/0004-637X/797/2/82)
- Lefor, A. T., Futamase, T., & Akhlaghi, M. 2013, *NewAR*, 57, 1, doi: [10.1016/j.newar.2013.05.001](https://doi.org/10.1016/j.newar.2013.05.001)
- Li, M., Bryan, G. L., & Ostriker, J. P. 2017, *ApJ*, 841, 101, doi: [10.3847/1538-4357/aa7263](https://doi.org/10.3847/1538-4357/aa7263)
- Li, N., Gladders, M. D., Heitmann, K., et al. 2019, *ApJ*, 878, 122, doi: [10.3847/1538-4357/ab1f74](https://doi.org/10.3847/1538-4357/ab1f74)
- Lynds, R., & Petrosian, V. 1986, in *Bulletin of the American Astronomical Society*, Vol. 18, 1014
- Markevitch, M., & Vikhlinin, A. 2007, *PhR*, 443, 1, doi: [10.1016/j.physrep.2007.01.001](https://doi.org/10.1016/j.physrep.2007.01.001)
- Martinez, M. N., Napier, K. A., Cloonan, A. P., et al. 2023, *ApJ*, 946, 63, doi: [10.3847/1538-4357/acbe39](https://doi.org/10.3847/1538-4357/acbe39)
- Meneghetti, M., Bartelmann, M., Dahle, H., & Limousin, M. 2013, *SSRv*, 177, 31, doi: [10.1007/s11214-013-9981-x](https://doi.org/10.1007/s11214-013-9981-x)
- Meneghetti, M., Natarajan, P., Coe, D., et al. 2017, *MNRAS*, 472, 3177, doi: [10.1093/mnras/stx2064](https://doi.org/10.1093/mnras/stx2064)
- Napier, K., Sharon, K., Dahle, H., et al. 2023a, *ApJ*, 959, 134, doi: [10.3847/1538-4357/ad045a](https://doi.org/10.3847/1538-4357/ad045a)
- Napier, K., Gladders, M. D., Sharon, K., et al. 2023b, *ApJL*, 954, L38, doi: [10.3847/2041-8213/acf132](https://doi.org/10.3847/2041-8213/acf132)
- Navarro, J. F., Frenk, C. S., & White, S. D. M. 1996, *ApJ*, 462, 563, doi: [10.1086/177173](https://doi.org/10.1086/177173)
- Oegerle, W. R., & Hoessel, J. G. 1991, *ApJ*, 375, 15, doi: [10.1086/170165](https://doi.org/10.1086/170165)
- Oguri, M. 2010, *PASJ*, 62, 1017, doi: [10.1093/pasj/62.4.1017](https://doi.org/10.1093/pasj/62.4.1017)

- Presotto, V., Girardi, M., Nonino, M., et al. 2014, *A&A*, 565, A126, doi: [10.1051/0004-6361/201323251](https://doi.org/10.1051/0004-6361/201323251)
- Remolina González, J. D., Sharon, K., Li, N., et al. 2021a, *ApJ*, 910, 146, doi: [10.3847/1538-4357/abe62a](https://doi.org/10.3847/1538-4357/abe62a)
- Remolina González, J. D., Sharon, K., Reed, B., et al. 2020, *ApJ*, 902, 44, doi: [10.3847/1538-4357/abb2a1](https://doi.org/10.3847/1538-4357/abb2a1)
- Remolina González, J. D., Sharon, K., Mahler, G., et al. 2021b, *ApJ*, 920, 98, doi: [10.3847/1538-4357/ac16d8](https://doi.org/10.3847/1538-4357/ac16d8)
- Rivera-Thorsen, T. E., Dahle, H., Gronke, M., et al. 2017, *A&A*, 608, L4, doi: [10.1051/0004-6361/201732173](https://doi.org/10.1051/0004-6361/201732173)
- Rojas, K., Savary, E., Clément, B., et al. 2022, *A&A*, 668, A73, doi: [10.1051/0004-6361/202142119](https://doi.org/10.1051/0004-6361/202142119)
- Rojas, K., Collett, T. E., Ballard, D., et al. 2023, *MNRAS*, 523, 4413, doi: [10.1093/mnras/stad1680](https://doi.org/10.1093/mnras/stad1680)
- Rubin, V. C. 1986, *Highlights of Astronomy*, 7, 27
- Schäfer, C., Fourestey, G., & Kneib, J. P. 2020, *Astronomy and Computing*, 30, 100360, doi: [10.1016/j.ascom.2019.100360](https://doi.org/10.1016/j.ascom.2019.100360)
- Shajib, A. J., Vernardos, G., Collett, T. E., et al. 2022, arXiv e-prints, arXiv:2210.10790, doi: [10.48550/arXiv.2210.10790](https://doi.org/10.48550/arXiv.2210.10790)
- Sharon, K., Bayliss, M. B., Dahle, H., et al. 2020, *ApJS*, 247, 12, doi: [10.3847/1538-4365/ab5f13](https://doi.org/10.3847/1538-4365/ab5f13)
- Sharon, K., Mahler, G., Rivera-Thorsen, T. E., et al. 2022, *ApJ*, 941, 203, doi: [10.3847/1538-4357/ac927a](https://doi.org/10.3847/1538-4357/ac927a)
- Soucail, G., Fort, B., Mellier, Y., & Picat, J. P. 1987, *A&A*, 172, L14
- Sukay, E., Khullar, G., Gladders, M. D., et al. 2022, *ApJ*, 940, 42, doi: [10.3847/1538-4357/ac9974](https://doi.org/10.3847/1538-4357/ac9974)
- Tran, K.-V. H., Harshan, A., Glazebrook, K., et al. 2022, *AJ*, 164, 148, doi: [10.3847/1538-3881/ac7da2](https://doi.org/10.3847/1538-3881/ac7da2)
- Virtanen, P., Gommers, R., Oliphant, T. E., et al. 2020, *Nature Methods*, 17, 261, doi: [10.1038/s41592-019-0686-2](https://doi.org/10.1038/s41592-019-0686-2)
- Wang, J., & Zhong, Z. 2018, *A&A*, 619, L1, doi: [10.1051/0004-6361/201834109](https://doi.org/10.1051/0004-6361/201834109)
- Wes McKinney. 2010, in *Proceedings of the 9th Python in Science Conference*, ed. Stéfan van der Walt & Jarrod Millman, 56 – 61, doi: [10.25080/Majora-92bf1922-00a](https://doi.org/10.25080/Majora-92bf1922-00a)
- White, M. 2001, *A&A*, 367, 27, doi: [10.1051/0004-6361:20000357](https://doi.org/10.1051/0004-6361:20000357)
- Zaborowski, E. A., Drlica-Wagner, A., Ashmead, F., et al. 2023, *ApJ*, 954, 68, doi: [10.3847/1538-4357/ace4ba](https://doi.org/10.3847/1538-4357/ace4ba)
- Zhang, Y., Manwadkar, V., Gladders, M. D., et al. 2023, *ApJ*, 950, 58, doi: [10.3847/1538-4357/acc9be](https://doi.org/10.3847/1538-4357/acc9be)
- Zhou, R., Ferraro, S., White, M., et al. 2023, *JCAP*, 2023, 097, doi: [10.1088/1475-7516/2023/11/097](https://doi.org/10.1088/1475-7516/2023/11/097)
- Zwicky, F. 1933, *Helvetica Physica Acta*, 6, 110

Table 2. Measured Quantities for all 177 Systems

ID	RA [°]	Dec [°]	z_{BCG}	θ_E ["]	$M_{\odot, \Sigma}$ [dex]	$M_{\odot, *}$ [dex]	L_{\odot} [dex]
J0008+1822 ^m	2.029829	18.372282	0.5566 ± 0.0483 ^P	3.2431 ± 0.1446	12.3479 ± 0.0594	11.2363 ± 0.0944	10.5378 ± 0.0835
J0008-0624 ^o	2.169667	-6.405227	0.9801 ± 0.0584 ^P	3.7217 ± 0.1170	12.7744 ± 0.0674	11.2099 ± 0.1202	10.7562 ± 0.0632
J0008+2150 ^m	2.181223	21.836401	0.5974 ± 0.0190 ^P	7.3602 ± 0.4852	13.0947 ± 0.0627	11.8165 ± 0.1114	10.9954 ± 0.0348
J0019+0438 ^m	4.954375	4.649355	0.8685 ± 0.0339 ^P	5.8885 ± 0.9581	13.1101 ± 0.1467	11.7218 ± 0.3601	11.0978 ± 0.0804
J0021+0333 ^m	5.402546	3.556039	0.7164 ± 0.0222 ^P	4.5494 ± 0.2190	12.7638 ± 0.0520	11.7067 ± 0.1184	10.9886 ± 0.0356
J0022+1431 ^o	5.670506	14.519566	0.3805 ± 0.0001 ^S	3.8254 ± 0.0599	12.3208 ± 0.0169	11.1673 ± 0.0893	10.7093 ± 0.0020
J0023-0252 ^o	5.835225	-2.874259	0.7973 ± 0.0698 ^P	2.0058 ± 0.2289	12.2348 ± 0.1202	10.8995 ± 0.0010	10.2946 ± 0.1102
J0027-0413 ^m	6.750411	-4.223259	0.4950 ± 0.0001 ^S	5.6052 ± 0.2712	12.7693 ± 0.0434	11.8215 ± 0.0886	11.0519 ± 0.0053
J0030-0101 ^o	7.558161	-1.029405	0.7234 ± 0.0954 ^P	3.6596 ± 0.4608	12.7085 ± 0.1409	11.1761 ± 0.2916	10.5556 ± 0.1754
J0032+0740 ^o	8.013587	7.667835	0.6437 ± 0.0003 ^S	3.0485 ± 0.2216	12.4813 ± 0.0674	11.5989 ± 0.1874	10.7664 ± 0.0158
J0034+0225 ^m	8.617335	2.422958	0.3865 ± 0.0077 ^P	13.3278 ± 0.7876	13.4127 ± 0.0525	11.8401 ± 0.1610	11.2355 ± 0.0213
J0036-0506 ^o	9.081628	-5.108834	0.8121 ± 0.0223 ^P	3.8970 ± 0.0943	12.6984 ± 0.0426	11.4701 ± 0.1397	10.9183 ± 0.0286
J0038+0719 ^m	9.730731	7.323072	0.2643 ± 0.0178 ^P	7.3590 ± 0.0588	12.7345 ± 0.0292	11.4604 ± 0.0443	10.7314 ± 0.0669
J0046-0156 ^m	11.508417	-1.941216	0.5501 ± 0.0002 ^S	5.3104 ± 0.3456	12.7713 ± 0.0588	11.6781 ± 0.1068	10.9179 ± 0.0072
J0047+0508 ^m	11.961840	5.138756	0.4291 ± 0.0001 ^S	8.9680 ± 0.1704	13.1134 ± 0.0209	11.7715 ± 0.1798	11.1678 ± 0.0063
J0051-0923 ^o	12.900786	-9.390354	0.7134 ± 0.0243 ^P	3.6019 ± 0.2007	12.5599 ± 0.0582	11.6749 ± 0.1024	11.0457 ± 0.0363
J0056-1402 ^m	14.247809	-14.042115	0.4251 ± 0.0208 ^P	6.1175 ± 0.3036	12.7791 ± 0.0501	11.5599 ± 0.1234	10.8910 ± 0.0535
J0057+2138 ^o	14.312163	21.642771	0.8471 ± 0.0402 ^P	4.0474 ± 0.0557	12.7556 ± 0.0470	11.5082 ± 0.0201	10.9451 ± 0.0550
J0057+0230 ^o	14.421865	2.504200	0.9262 ± 0.0005 ^S	3.8478 ± 0.1220	12.7632 ± 0.0473	11.6204 ± 0.1193	11.0455 ± 0.0074
J0058-0721 ^m	14.703994	-7.365765	0.6379 ± 0.0001 ^S	15.5906 ± 0.5102	13.7754 ± 0.0354	12.4146 ± 0.0888	11.6556 ± 0.0036
J0100+1818 ^o	15.204935	18.307730	0.5819 ± 0.0002 ^S	6.3332 ± 0.5963	13.0701 ± 0.0821	11.8056 ± 0.1124	10.9924 ± 0.0077
J0101+2055 ^o	15.437768	20.928614	0.8708 ± 0.0003 ^S	4.5847 ± 0.1863	12.8807 ± 0.0494	11.5800 ± 0.1037	10.8803 ± 0.0171
J0101-2126 ^o	15.498254	-21.448722	0.4001 ± 0.0375 ^P	4.4222 ± 0.2826	12.4691 ± 0.0694	11.6006 ± 0.1268	10.8508 ± 0.0965
J0102-1400 ^o	15.676298	-14.015030	0.6737 ± 0.0321 ^P	3.5777 ± 0.0469	12.6385 ± 0.0338	11.3892 ± 0.0428	10.8223 ± 0.0492
J0102-2356 ^o	15.678569	-23.943939	0.7084 ± 0.0286 ^P	3.1461 ± 0.0379	12.4376 ± 0.0332	11.2482 ± 0.1321	10.6643 ± 0.0430
J0103+2706 ^m	15.937230	27.102542	0.3825 ± 0.0001 ^S	4.3067 ± 0.5513	12.5506 ± 0.1105	11.5542 ± 0.1512	10.7612 ± 0.0282
J0104-0340 ^o	16.214582	-3.671084	0.9163 ± 0.0350 ^P	6.8895 ± 0.0476	13.2638 ± 0.0492	11.3674 ± 0.1768	11.1311 ± 0.0442
J0104-0757 ^o	16.220190	-7.952046	0.8988 ± 0.0401 ^P	2.6289 ± 0.1924	12.4196 ± 0.0831	11.3152 ± 0.1311	10.8239 ± 0.0505
J0105-0501 ^o	16.462922	-5.032347	0.7015 ± 0.0002 ^S	3.7470 ± 0.0744	12.5842 ± 0.0294	11.6409 ± 0.0585	11.0437 ± 0.0028
J0109-0455 ^m	17.294557	-4.919535	0.7623 ± 0.0352 ^P	5.1460 ± 0.1236	12.9069 ± 0.0439	11.7990 ± 0.1102	11.1524 ± 0.0473
J0109-3335 ^m	17.469499	-33.592604	0.4730 ± 0.0114 ^P	9.0865 ± 0.1633	13.1676 ± 0.0239	11.9410 ± 0.0867	11.2692 ± 0.0259
J0111+1346 ^m	17.779877	13.778901	0.7203 ± 0.0002 ^S	5.2451 ± 0.9923	12.9065 ± 0.1627	11.7728 ± 0.3236	11.1351 ± 0.0841
J0111+0855 ^m	17.881205	8.928360	0.4855 ± 0.0001 ^S	11.2303 ± 0.3733	13.3637 ± 0.0327	12.1471 ± 0.1127	11.4398 ± 0.0110
J0112-2053 ^m	18.014632	-20.891104	0.6441 ± 0.0355 ^P	5.4284 ± 0.3018	12.8648 ± 0.0595	11.9186 ± 0.1656	11.2702 ± 0.0612
J0117-0527 ^m	19.494867	-5.454945	0.5797 ± 0.0002 ^S	2.8465 ± 0.2686	12.3730 ± 0.0814	11.3386 ± 0.1937	10.6179 ± 0.0259
J0118-0526 ^m	19.663276	-5.443448	0.5803 ± 0.0002 ^S	12.8405 ± 0.1036	13.5613 ± 0.0193	12.1258 ± 0.0706	11.4273 ± 0.0033
J0122-0831 ^o	20.604365	-8.520537	0.4906 ± 0.0495 ^P	2.0523 ± 0.2209	12.0154 ± 0.1054	11.0911 ± 0.1386	10.4452 ± 0.1081
J0124-2401 ^o	21.086027	-24.029980	0.6187 ± 0.0092 ^P	2.9426 ± 0.1948	12.3140 ± 0.0608	11.6559 ± 0.1861	10.9180 ± 0.0192
J0127+2713 ^m	21.939205	27.229009	0.7989 ± 0.0234 ^P	7.1353 ± 0.3294	13.2140 ± 0.0522	11.9420 ± 0.0511	11.3248 ± 0.0325
J0130-0305 ^m	22.517741	-3.095758	0.6754 ± 0.1767 ^P	17.8274 ± 0.2720	13.9264 ± 0.1399	12.5665 ± 0.0855	11.6481 ± 0.3212
J0130+3216 ^o	22.730273	32.275463	0.5093 ± 0.0001 ^S	9.5797 ± 0.8274	13.3667 ± 0.0753	11.5566 ± 0.0884	10.9050 ± 0.0070
J0133-1650 ^m	23.423964	-16.839019	0.6490 ± 0.0191 ^P	6.1055 ± 0.5181	12.9727 ± 0.0784	11.5655 ± 0.1746	11.0693 ± 0.0423
J0134+0433 ^o	23.676569	4.563916	0.5509 ± 0.0001 ^S	5.2927 ± 0.1836	12.8849 ± 0.0357	11.7604 ± 0.0564	11.0052 ± 0.0039
J0135-2033 ^m	23.928317	-20.559902	0.6111 ± 0.0169 ^P	4.7364 ± 0.3760	12.8403 ± 0.0737	11.8398 ± 0.1447	11.1292 ± 0.0305
J0136-2200 ^o	24.211948	-22.007600	0.6741 ± 0.0247 ^P	2.6192 ± 0.1161	12.3702 ± 0.0491	11.4187 ± 0.1177	10.6767 ± 0.0446
J0137+2109 ^o	24.385656	21.156756	0.8805 ± 0.0610 ^P	4.4567 ± 0.5514	12.9894 ± 0.1220	11.2638 ± 0.2091	10.9060 ± 0.0742
J0138-2155 ^m	24.515695	-21.925493	0.2468 ± 0.0451 ^P	18.2693 ± 0.4811	13.4977 ± 0.0793	12.0640 ± 0.0339	11.1297 ± 0.1897
J0138-2844 ^m	24.597416	-28.735794	0.4005 ± 0.0141 ^P	8.7725 ± 0.1847	13.0635 ± 0.0260	11.6350 ± 0.1838	10.9807 ± 0.0406
J0139+2207 ^o	24.778355	22.123106	0.4770 ± 0.0001 ^S	5.8602 ± 0.4416	12.7931 ± 0.0670	11.5957 ± 0.0918	10.8865 ± 0.0083
J0140-2006 ^m	25.052071	-20.105520	0.3617 ± 0.0070 ^P	17.3092 ± 0.8612	13.6105 ± 0.0447	11.9248 ± 0.1966	11.2967 ± 0.0212
J0143+1427 ^o	25.953318	14.461970	0.3305 ± 0.0001 ^S	6.8998 ± 0.3140	12.7743 ± 0.0408	11.3398 ± 0.2162	10.6899 ± 0.0034
J0144-2213 ^m	26.168407	-22.229454	0.2773 ± 0.0068 ^P	12.5538 ± 0.0634	13.2187 ± 0.0130	11.8627 ± 0.0364	11.0659 ± 0.0255

Table 2 continued

Table 2 (continued)

ID	RA [°]	Dec [°]	z_{BCG}	θ_E ["]	$M_{\odot, \Sigma}$ [dex]	$M_{\odot, *}$ [dex]	L_{\odot} [dex]
J0144+1008 °	26.172042	10.141264	0.4649 ± 0.0001 ^S	4.1770 ± 0.1607	12.4857 ± 0.0358	11.3946 ± 0.1086	10.7550 ± 0.0056
J0145-3541 °	26.444968	-35.691008	0.4986 ± 0.0182 ^P	3.7835 ± 0.0985	12.4300 ± 0.0328	11.4321 ± 0.0631	10.7235 ± 0.0413
J0145+0402 °	26.484783	4.041294	0.7800 ± 0.0410 ^P	2.2780 ± 0.0877	12.3276 ± 0.0560	11.3770 ± 0.1367	10.7692 ± 0.0568
J0146-0929 ^m *	26.733372	-9.497905	0.4469 ± 0.0001 ^S	12.1801 ± 0.5248	13.5148 ± 0.0396	12.0644 ± 0.0874	11.3973 ± 0.0034
J0149-2834 °	27.483033	-28.575331	0.5563 ± 0.0076 ^P	5.8990 ± 0.1144	12.8664 ± 0.0254	11.6969 ± 0.0422	10.9577 ± 0.0154
J0150+2725 ^m	27.503618	27.426752	0.3062 ± 0.0001 ^S	5.5224 ± 0.3406	12.5492 ± 0.0548	11.5340 ± 0.0749	10.7487 ± 0.0069
J0151-0407 ^m	27.908847	-4.120915	0.6700 ± 0.0002 ^S	6.7660 ± 0.1959	13.0749 ± 0.0342	11.9359 ± 0.1096	11.1376 ± 0.0060
J0153-3235 °	28.474812	-32.599633	0.6541 ± 0.0204 ^P	4.1855 ± 0.0550	12.6452 ± 0.0295	11.5416 ± 0.1301	10.9411 ± 0.0345
J0159-3413 ^m	29.766637	-34.217907	0.4143 ± 0.0252 ^P	10.4481 ± 0.1989	13.2293 ± 0.0323	11.8191 ± 0.1728	11.2005 ± 0.0679
J0202-1109 ^m *	30.543766	-11.153215	0.4444 ± 0.0237 ^P	5.6519 ± 0.7326	12.8526 ± 0.1131	11.6920 ± 0.1024	10.9192 ± 0.0545
J0203-2017 ^m	30.793373	-20.289939	0.4389 ± 0.0227 ^P	13.3912 ± 0.4259	13.4719 ± 0.0375	11.9077 ± 0.1197	11.2031 ± 0.0590
J0204-2918 ^m	31.034313	-29.302323	0.9894 ± 0.0775 ^P	3.9745 ± 0.0540	12.8406 ± 0.0737	11.4984 ± 0.2316	11.0811 ± 0.0955
J0205-3539 ^m	31.358759	-35.663177	0.3856 ± 0.0101 ^P	3.4782 ± 0.0561	12.2441 ± 0.0211	11.3942 ± 0.0211	10.7298 ± 0.0274
J0209-3547 ^m	32.476474	-35.799023	0.3105 ± 0.0097 ^P	5.8527 ± 0.4780	12.6069 ± 0.0724	11.5478 ± 0.0768	10.7458 ± 0.0324
J0210+2600 °	32.594801	26.011166	0.3960 ± 0.0001 ^S	3.2755 ± 0.0630	12.2030 ± 0.0195	11.2954 ± 0.0693	10.7267 ± 0.0022
J0210+3044 °	32.744179	30.739885	0.4687 ± 0.1181 ^P	5.5256 ± 0.9274	12.7561 ± 0.1985	11.4055 ± 0.1522	10.7429 ± 0.3074
J0214-0206 ^o *	33.533392	-2.107933	0.6477 ± 0.0322 ^P	2.9225 ± 0.2936	12.4520 ± 0.0920	11.5662 ± 0.1695	10.8001 ± 0.0587
J0224+0849 ^o *	36.233942	8.829935	0.3271 ± 0.0225 ^P	7.6845 ± 0.3879	12.8637 ± 0.0533	11.8480 ± 0.1421	11.1563 ± 0.0718
J0225-0737 ^m	36.442200	-7.627366	0.5137 ± 0.0001 ^S	6.2327 ± 0.4870	12.8795 ± 0.0701	11.6916 ± 0.1246	10.9776 ± 0.0172
J0227+2934 ^m *	36.806665	29.579592	0.4856 ± 0.0351 ^P	3.9666 ± 0.5623	12.5866 ± 0.1266	11.3633 ± 0.1055	10.6706 ± 0.0800
J0228-2923 °	37.067992	-29.396016	0.2951 ± 0.0106 ^P	3.8286 ± 0.2142	12.2159 ± 0.0513	11.2861 ± 0.0695	10.4456 ± 0.0382
J0230-2702 ^m	37.702673	-27.041580	0.3874 ± 0.0330 ^P	13.3375 ± 0.4507	13.4144 ± 0.0487	11.5716 ± 0.1364	10.9715 ± 0.1014
J0233+0559 ^m	38.348967	5.999309	0.2688 ± 0.0122 ^P	13.0853 ± 0.1110	13.2416 ± 0.0214	12.0689 ± 0.0758	11.2812 ± 0.0479
J0233+0642 °	38.488527	6.711545	0.5972 ± 0.0179 ^P	2.9543 ± 0.1346	12.3010 ± 0.0465	11.4323 ± 0.0624	10.7955 ± 0.0341
J0237-3017 ^m	39.348438	-30.292085	0.5451 ± 0.0182 ^P	5.3818 ± 0.2927	12.7783 ± 0.0528	11.7743 ± 0.0951	11.0858 ± 0.0375
J0239-2047 °	39.776954	-20.788370	0.6268 ± 0.0098 ^P	3.6113 ± 0.0629	12.4961 ± 0.0266	11.7599 ± 0.0719	10.9720 ± 0.0175
J0239-0134 ^m	39.971351	-1.582259	0.3731 ± 0.0001 ^S	11.2100 ± 0.6935	13.2480 ± 0.0549	11.8979 ± 0.1383	11.2710 ± 0.0079
J0248-0216 ^m	42.034802	-2.276981	0.2338 ± 0.0000 ^S	13.3201 ± 0.2057	13.1984 ± 0.0144	11.8312 ± 0.0675	11.0657 ± 0.0023
J0251-1220 ^m	42.897099	-12.333713	0.4324 ± 0.0123 ^P	5.1718 ± 0.2473	12.6387 ± 0.0454	11.5625 ± 0.1004	10.8641 ± 0.0331
J0251-2358 °	42.990479	-23.978480	0.3488 ± 0.0075 ^P	11.5719 ± 0.0731	13.2453 ± 0.0140	11.8767 ± 0.0078	11.2202 ± 0.0213
J0255-1640 ^m	43.821469	-16.681517	0.6949 ± 0.0251 ^P	3.5382 ± 0.0561	12.5302 ± 0.0343	11.3902 ± 0.0480	10.8106 ± 0.0405
J0257-2008 ^m	44.433800	-20.147361	0.7033 ± 0.0214 ^P	5.5778 ± 0.0402	12.9304 ± 0.0303	11.9830 ± 0.0824	11.2537 ± 0.0350
J0302-1004 ^m	45.597783	-10.076458	0.5506 ± 0.0644 ^P	17.7556 ± 0.4175	13.8200 ± 0.0621	12.1914 ± 0.1028	11.5761 ± 0.1323
J0303-2119 ^m	45.791775	-21.325857	0.4059 ± 0.0176 ^P	11.3597 ± 0.0991	13.2944 ± 0.0234	11.6924 ± 0.0288	11.1592 ± 0.0442
J0310-1746 ^o *	47.708730	-17.774793	0.6691 ± 0.0524 ^P	2.7874 ± 0.1736	12.3081 ± 0.0716	11.4130 ± 0.1711	10.6386 ± 0.0873
J0318-2915 ^m	49.619953	-29.259311	0.5432 ± 0.0246 ^P	4.7809 ± 0.1150	12.7895 ± 0.0351	11.6384 ± 0.0769	10.8987 ± 0.0514
J0327-1326 ^m *	51.863245	-13.439585	0.5759 ± 0.0230 ^P	21.3502 ± 2.8938	14.0070 ± 0.1226	12.4358 ± 0.2426	11.7787 ± 0.0585
J0328-2140 ^m	52.056629	-21.672094	0.5617 ± 0.0125 ^P	19.9614 ± 1.3808	13.9311 ± 0.0611	12.5000 ± 0.1279	11.8501 ± 0.0283
J0334-1311 ^o *	53.625432	-13.186562	0.3622 ± 0.0121 ^P	6.7750 ± 1.1623	12.9257 ± 0.1453	11.7358 ± 0.1275	10.9468 ± 0.0392
J0340-2533 ^m	55.089050	-25.558420	0.6326 ± 0.0189 ^P	3.6340 ± 0.3239	12.6255 ± 0.0803	11.4958 ± 0.1199	10.7713 ± 0.0336
J0347-2454 °	56.935631	-24.908777	0.6390 ± 0.0350 ^P	2.6813 ± 0.1082	12.3657 ± 0.0499	11.4301 ± 0.0796	10.7615 ± 0.0627
J0348-2145 ^m	57.009695	-21.750889	0.3565 ± 0.0173 ^P	9.3239 ± 0.9232	13.0714 ± 0.0862	11.9305 ± 0.1862	11.1878 ± 0.0612
J0349-1500 °	57.450133	-15.002336	0.3212 ± 0.0086 ^P	6.8526 ± 0.3801	12.7568 ± 0.0503	11.6309 ± 0.0772	10.8348 ± 0.0284
J0353-1706 °	58.442671	-17.110893	0.5256 ± 0.0904 ^P	2.0505 ± 0.0567	12.0426 ± 0.0862	11.3743 ± 0.0267	10.4374 ± 0.1943
J0354-1609 ^o *	58.576148	-16.164544	0.5887 ± 0.0082 ^P	2.5302 ± 0.2045	12.2775 ± 0.0718	11.5293 ± 0.0750	10.8251 ± 0.0165
J0400-1357 ^m	60.241996	-13.956629	0.6457 ± 0.0335 ^P	11.0343 ± 0.6570	13.4828 ± 0.0620	11.9998 ± 0.1808	11.2753 ± 0.0591
J0401-0951 °	60.314572	-9.860522	0.5816 ± 0.1755 ^P	3.6236 ± 0.0457	12.5847 ± 0.1502	11.7039 ± 0.0034	10.6573 ± 0.4109
J0411-2256 ^m	62.783524	-22.944009	0.4954 ± 0.0267 ^P	4.7790 ± 0.2868	12.6303 ± 0.0589	11.6568 ± 0.1454	10.9039 ± 0.0643
J0420-0421 °	65.242499	-4.357444	0.7245 ± 0.0421 ^P	3.0239 ± 0.1457	12.5342 ± 0.0589	11.5643 ± 0.1256	10.8291 ± 0.0683
J0423-0121 °	65.796719	-1.351486	0.3851 ± 0.0245 ^P	3.8175 ± 0.1122	12.3238 ± 0.0398	11.3825 ± 0.0938	10.7479 ± 0.0666
J0424-1624 °	66.011723	-16.411331	0.6681 ± 0.0379 ^P	2.8343 ± 0.1562	12.4363 ± 0.0595	11.4788 ± 0.1160	10.7444 ± 0.0678
J0424-3317 ^o *	66.161195	-33.294925	0.5542 ± 0.0594 ^P	4.9734 ± 0.4561	12.8353 ± 0.0941	11.9122 ± 0.1256	11.1048 ± 0.1203
J0429-2957 ^m	67.472905	-29.959746	0.6919 ± 0.0195 ^P	11.7104 ± 0.3467	13.5683 ± 0.0385	11.9433 ± 0.0361	11.3918 ± 0.0306
J0432-2000 °	68.102241	-20.003820	0.5642 ± 0.0164 ^P	4.3046 ± 0.3815	12.6016 ± 0.0798	11.6363 ± 0.0893	10.9457 ± 0.0326

Table 2 continued

Table 2 (continued)

ID	RA [°]	Dec [°]	z_{BCG}	θ_E ["]	$M_{\odot, \Sigma}$ [dex]	$M_{\odot, *}$ [dex]	L_{\odot} [dex]
J0440-2658 ^m	70.192758	-26.975392	0.5018 ± 0.0089 ^P	9.9881 ± 0.4193	13.2767 ± 0.0407	11.8938 ± 0.0935	11.2158 ± 0.0194
J0447-0251 ^m	71.865678	-2.861248	0.4270 ± 0.0104 ^P	10.4768 ± 2.7785	13.2751 ± 0.2313	11.9119 ± 0.4235	11.1838 ± 0.1023
J0450-3302 ^m	72.501915	-33.048279	0.4990 ± 0.0158 ^P	6.7920 ± 0.1347	12.9391 ± 0.0282	11.7887 ± 0.0739	11.0779 ± 0.0346
J0451+0006 ^{m*}	72.977704	0.105035	0.4221 ± 0.0171 ^P	35.8005 ± 2.0949	14.3096 ± 0.0543	12.4608 ± 0.1270	11.7802 ± 0.0443
J0452-3540 ^o	73.123877	-35.674171	0.5958 ± 0.0123 ^P	2.9425 ± 0.0674	12.2948 ± 0.0297	11.4572 ± 0.0617	10.7358 ± 0.0234
J0455-2530 ^{m*}	73.903064	-25.512814	0.3524 ± 0.0374 ^P	15.9619 ± 0.1962	13.5310 ± 0.0466	11.5990 ± 0.0950	11.0584 ± 0.1182
J0458-2637 ^m	74.673306	-26.626873	0.2677 ± 0.0075 ^P	11.3630 ± 0.0540	13.1170 ± 0.0141	11.6874 ± 0.0440	10.9491 ± 0.0298
J0459-3043 ^m	74.964252	-30.723626	0.4329 ± 0.0106 ^P	3.5759 ± 0.0773	12.3176 ± 0.0256	11.3325 ± 0.1536	10.6898 ± 0.0261
J0513-3050 ^m	78.356121	-30.843339	0.3814 ± 0.0152 ^P	5.4548 ± 0.4222	12.6330 ± 0.0698	11.5392 ± 0.1286	10.8729 ± 0.0435
J0524-2721 ^m	81.098605	-27.353147	0.3081 ± 0.0086 ^P	6.8557 ± 0.2129	12.7382 ± 0.0305	11.6347 ± 0.0617	10.8221 ± 0.0283
J0527-1858 ^{m*}	81.754744	-18.967375	0.4420 ± 0.0116 ^P	7.3056 ± 0.7421	13.0698 ± 0.0909	11.7325 ± 0.1197	11.0333 ± 0.0279
J0532-3545 ^m	83.077550	-35.755547	0.4924 ± 0.0313 ^P	5.3516 ± 0.0409	12.7244 ± 0.0330	11.5158 ± 0.0511	10.7890 ± 0.0736
J0545-2635 ^{m*}	86.306565	-26.588383	0.3177 ± 0.0220 ^P	13.3576 ± 0.0791	13.3303 ± 0.0300	11.8456 ± 0.0523	11.3718 ± 0.0717
J0545-3542 ^o	86.352690	-35.714575	0.4065 ± 0.0086 ^P	10.8589 ± 0.2087	13.2555 ± 0.0218	11.4552 ± 0.0915	10.9562 ± 0.0207
J0549-2355 ^m	87.402875	-23.925304	0.5165 ± 0.0114 ^P	5.7656 ± 0.6057	12.8166 ± 0.0933	11.8464 ± 0.2017	11.1332 ± 0.0394
J0553-2853 ^o	88.296789	-28.893375	0.7899 ± 0.0617 ^P	2.3562 ± 0.1271	12.3668 ± 0.0713	11.0630 ± 0.0692	10.6426 ± 0.0863
J0559-3540 ^{o*}	89.956356	-35.670137	0.8034 ± 0.0381 ^P	2.4366 ± 0.2014	12.4059 ± 0.0836	11.4305 ± 0.1689	10.9083 ± 0.0549
J1132+0212 ^{o*}	173.111909	2.215971	0.9367 ± 0.0505 ^P	10.4815 ± 1.2337	13.6499 ± 0.1132	11.5785 ± 0.2362	11.2598 ± 0.0688
J2043-0609 ^o	310.801950	-6.164955	0.8125 ± 0.0385 ^P	4.9276 ± 0.3242	12.9029 ± 0.0696	11.7136 ± 0.1030	11.1461 ± 0.0547
J2105+0537 ^m	316.420521	5.620318	0.3095 ± 0.0179 ^P	5.5740 ± 0.2132	12.5583 ± 0.0421	11.8041 ± 0.1454	11.0545 ± 0.0608
J2106-0027 ^m	316.613480	-0.458322	0.7903 ± 0.0313 ^P	7.2086 ± 0.3762	13.2184 ± 0.0578	11.8610 ± 0.1772	11.3299 ± 0.0474
J2106-0547 ^m	316.721396	-5.783672	0.6485 ± 0.0501 ^P	3.8671 ± 0.9094	12.7110 ± 0.2080	11.5791 ± 0.2754	10.8871 ± 0.1047
J2109-0135 ^o	317.329931	-1.593868	0.8934 ± 0.0533 ^P	1.5025 ± 0.2300	11.9386 ± 0.1480	11.2400 ± 0.2550	10.6351 ± 0.0905
J2111-0114 ^{m*}	317.830618	-1.239845	0.6386 ± 0.0001 ^S	12.6252 ± 1.5331	13.6005 ± 0.1091	12.1776 ± 0.2164	11.4900 ± 0.0365
J2114+0658 ^m	318.724767	6.968209	0.2081 ± 0.0052 ^P	8.1851 ± 0.4026	12.7274 ± 0.0449	11.5598 ± 0.0657	10.7503 ± 0.0249
J2126+0949 ^o	321.560372	9.833233	0.8025 ± 0.0291 ^P	4.1700 ± 0.4403	12.8715 ± 0.1005	11.5284 ± 0.1658	10.9920 ± 0.0414
J2129-0126 ^m	322.287133	-1.442114	0.9581 ± 0.0949 ^P	17.5086 ± 0.0426	14.1089 ± 0.0852	11.4555 ± 0.2358	11.3166 ± 0.1092
J2143+1431 ^m	325.794687	14.522257	0.4102 ± 0.0087 ^P	9.4940 ± 0.1068	13.1423 ± 0.0184	11.6014 ± 0.0376	11.0261 ± 0.0239
J2146-0317 ^m	326.623059	-3.284784	0.5759 ± 0.0213 ^P	12.3640 ± 0.0691	13.5257 ± 0.0263	11.4957 ± 0.0066	11.2704 ± 0.0395
J2151-0138 ^m	327.858149	-1.647066	0.3131 ± 0.0001 ^S	15.9036 ± 0.0759	13.4753 ± 0.0092	11.8579 ± 0.0111	11.3326 ± 0.0007
J2206+1104 ^o	331.567919	11.068702	0.7772 ± 0.0002 ^S	2.8576 ± 0.0721	12.4034 ± 0.0368	11.8932 ± 0.0826	11.0847 ± 0.0063
J2207-0411 ^{o*}	331.762532	-4.196620	0.7576 ± 0.0416 ^P	3.5709 ± 0.3867	12.7045 ± 0.1044	11.3932 ± 0.1781	10.9579 ± 0.0641
J2210+2604 ^m	332.512025	26.068904	0.3467 ± 0.0001 ^S	7.4681 ± 0.2191	12.8627 ± 0.0274	11.7072 ± 0.0743	10.8734 ± 0.0027
J2222+2745 ^m	335.536310	27.759241	0.4717 ± 0.0404 ^P	7.4138 ± 0.6700	12.9932 ± 0.0919	12.0060 ± 0.1049	11.2401 ± 0.0919
J2226+0041 ^m	336.538789	0.694997	0.6471 ± 0.0001 ^S	3.1267 ± 0.0892	12.3873 ± 0.0336	11.8505 ± 0.0510	10.9511 ± 0.0024
J2234-0630 ^{o*}	338.724911	-6.515025	0.8146 ± 0.0705 ^P	2.5836 ± 0.2115	12.4661 ± 0.0982	11.4292 ± 0.2681	10.7640 ± 0.1104
J2238+1319 ^{m*}	339.630481	13.332188	0.4129 ± 0.0001 ^S	9.3281 ± 0.2308	13.2479 ± 0.0237	11.8539 ± 0.1052	11.3099 ± 0.0024
J2240-0139 ^o	340.054725	-1.659645	0.8515 ± 0.0393 ^P	8.3870 ± 0.5461	13.3927 ± 0.0687	11.4458 ± 0.1560	10.9993 ± 0.0549
J2241-0527 ^m	340.298713	-5.460154	0.9632 ± 0.0418 ^P	8.2405 ± 0.1584	13.4557 ± 0.0596	12.2401 ± 0.2411	11.4152 ± 0.0496
J2244+2759 ^o	341.020635	27.987671	0.3429 ± 0.0001 ^S	6.1671 ± 0.2461	12.6916 ± 0.0357	11.7689 ± 0.0444	10.9261 ± 0.0045
J2246+0415 ^o	341.687109	4.263947	1.0241 ± 0.0503 ^P	9.6721 ± 0.3324	13.6355 ± 0.0783	11.5978 ± 0.1415	11.3445 ± 0.0549
J2247-0205 ^m	341.801229	-2.093837	0.3383 ± 0.0234 ^P	8.7594 ± 0.1647	12.9912 ± 0.0346	11.7359 ± 0.1764	11.1032 ± 0.0697
J2248-0123 ^m	342.151533	-1.392814	0.3983 ± 0.0001 ^S	4.1601 ± 0.1096	12.4137 ± 0.0256	11.2435 ± 0.0853	10.6479 ± 0.0021
J2248+2015 ^o	342.151611	20.252945	0.8046 ± 0.0320 ^P	4.0530 ± 0.0779	12.7274 ± 0.0433	11.5123 ± 0.1199	11.0254 ± 0.0442
J2249-0110 ^o	342.410083	-1.179021	0.3399 ± 0.0001 ^S	4.3647 ± 0.1033	12.3878 ± 0.0227	11.3617 ± 0.0476	10.5159 ± 0.0026
J2252-0413 ^m	343.040271	-4.218693	0.4273 ± 0.0139 ^P	7.5002 ± 0.1272	12.9566 ± 0.0231	11.7065 ± 0.0879	11.0875 ± 0.0333
J2256+1005 ^m	344.205409	10.086293	0.8824 ± 0.0395 ^P	7.3106 ± 0.4774	13.2962 ± 0.0748	11.6659 ± 0.1212	11.2499 ± 0.0519
J2257-0610 ^{o*}	344.434506	-6.173864	0.7776 ± 0.0335 ^P	5.1725 ± 0.2591	12.9198 ± 0.0577	11.5310 ± 0.1716	10.9212 ± 0.0471
J2258+1709 ^m	344.556726	17.150617	0.7990 ± 0.0413 ^P	8.5561 ± 0.1622	13.3714 ± 0.0483	11.9105 ± 0.1594	11.4468 ± 0.0633
J2259+1212 ^m	344.797839	12.209790	0.8885 ± 0.1309 ^P	4.8219 ± 0.3680	13.0569 ± 0.1227	11.8003 ± 0.1218	10.9898 ± 0.1751
J2300+2213 ^m	345.071926	22.224908	0.4237 ± 0.0116 ^P	17.8867 ± 0.1814	13.7078 ± 0.0193	12.0469 ± 0.1640	11.4679 ± 0.0296
J2303+2328 ^m	345.860959	23.475984	0.2767 ± 0.0000 ^S	9.0970 ± 0.3456	12.9388 ± 0.0339	11.6889 ± 0.0700	10.9067 ± 0.0057
J2304+3327 ^{o*}	346.022626	33.459947	0.4837 ± 0.0233 ^P	7.5387 ± 0.9608	13.0212 ± 0.1116	11.7765 ± 0.1300	11.0498 ± 0.0539
J2304-0052 ^m	346.101457	-0.877417	0.8850 ± 0.0305 ^P	4.9030 ± 0.2141	12.9480 ± 0.0572	11.7937 ± 0.0456	11.1501 ± 0.0375

Table 2 continued

Table 2 (*continued*)

ID	RA [°]	Dec [°]	z_{BCG}	θ_E ["]	$M_{\odot, \Sigma}$ [dex]	$M_{\odot, *}$ [dex]	L_{\odot} [dex]
J2307-1322 ^m *	346.766785	-13.374414	0.5087 ± 0.0223 ^P	7.6014 ± 0.1203	13.0455 ± 0.0288	11.8918 ± 0.0323	11.1448 ± 0.0535
J2308-0211 ^m	347.092613	-2.192172	0.2949 ± 0.0097 ^P	37.4958 ± 1.4818	14.1956 ± 0.0379	12.3708 ± 0.1143	11.6313 ± 0.0342
J2312+0451 ^m	348.245242	4.861479	0.3102 ± 0.0001 ^S	9.5915 ± 0.1157	13.0323 ± 0.0132	11.7486 ± 0.0834	10.9586 ± 0.0038
J2313-0104 ^m	348.477049	-1.080103	0.5312 ± 0.0002 ^S	7.8648 ± 0.2229	13.0941 ± 0.0286	11.8258 ± 0.0711	11.0930 ± 0.0036
J2318-1106 ^o	349.549151	-11.101265	0.7203 ± 0.0264 ^P	5.4290 ± 0.0264	12.9220 ± 0.0344	11.7873 ± 0.0336	11.1669 ± 0.0426
J2319+0038 ^m	349.972629	0.637053	0.8295 ± 0.1561 ^P	8.8106 ± 1.5057	13.4456 ± 0.1916	12.0224 ± 0.4035	11.4651 ± 0.2497
J2320-1202 ^m	350.027080	-12.034294	0.3967 ± 0.0130 ^P	5.6273 ± 0.2854	12.6744 ± 0.0472	11.6153 ± 0.1509	10.8922 ± 0.0433
J2326+2026 ^m	351.748351	20.449553	0.7895 ± 0.0289 ^P	5.7747 ± 0.4179	13.0236 ± 0.0739	11.8390 ± 0.1464	11.1600 ± 0.0452
J2331+2749 ^m	352.825967	27.817418	0.8688 ± 0.0618 ^P	9.5331 ± 0.1430	13.5153 ± 0.0609	11.1560 ± 0.0429	11.1953 ± 0.0841
J2334-0746 ^o	353.528695	-7.771200	0.4018 ± 0.0130 ^P	5.6332 ± 0.2861	12.6809 ± 0.0476	11.4592 ± 0.1648	10.7858 ± 0.0340
J2335+0922 ^o	353.981202	9.382482	0.7536 ± 0.0302 ^P	6.6253 ± 0.0521	13.1183 ± 0.0368	11.3639 ± 0.0546	10.9481 ± 0.0437
J2347-0047 ^m	356.811434	-0.797979	0.7889 ± 0.0188 ^P	8.1719 ± 0.1422	13.3231 ± 0.0377	11.9225 ± 0.1335	11.3496 ± 0.0262
J2347-0439 ^o	356.954863	-4.650060	0.9785 ± 0.0842 ^P	2.7133 ± 0.0469	12.5039 ± 0.0822	11.1439 ± 0.2992	10.7868 ± 0.1018
J2348+1407 ^o	357.034778	14.129527	0.6546 ± 0.0002 ^S	2.4746 ± 0.3247	12.3132 ± 0.1142	11.5998 ± 0.0877	10.7861 ± 0.0129
J2356+0241 ^o	359.142118	2.692205	0.8204 ± 0.0304 ^P	5.0113 ± 1.1522	13.0628 ± 0.2042	11.3861 ± 0.3399	10.8535 ± 0.0555
J2359-1214 ^m	359.802678	-12.236703	0.9131 ± 0.0672 ^P	7.4654 ± 0.1480	13.3350 ± 0.0684	11.5590 ± 0.2083	11.2256 ± 0.0836
J2359+0208 ^m *	359.889762	2.139947	0.4294 ± 0.0001 ^S	9.8445 ± 0.7516	13.1967 ± 0.0669	12.1698 ± 0.1299	11.4403 ± 0.0098

NOTE—All values quoted in dex are constrained exclusively within the Einstein aperture for each system. Luminosity was measured within the rest-frame wavelength interval of 3000Å to 7000Å. Superscript labels in the ID column stand for the following: ‘o’ and ‘m’ stand for whether one or multiple cluster members fall within the Einstein aperture respectively. Subscript asterisks in the ID column denote systems which were analyzed with LENSTOOL in Section 5.3. Superscript labels in the z_{BCG} column stand for the following: ‘p’ stands for LS DR9 photometric redshift; ‘s’ stands for SDSS DR15 spectroscopic redshift. A csv file containing the information in this table can be provided upon request to the corresponding author.

All Authors and Affiliations

SIMON D. MORK ¹ MICHAEL D. GLADDERS ^{1,2} GOURAV KHULLAR ^{3,4} KEREN SHARON ⁵
NATHALIE CHICOINE ¹ AIDAN P. CLOONAN ^{1,6} HÅKON DAHLE ⁷ DIEGO GARZA ^{1,8} ROWEN GLUSMAN ^{1,9}
KATYA GOZMAN ^{1,10} GABRIELA HORWATH ¹ BENJAMIN C. LEVINE ^{1,11} OLINA LIANG,¹ DANIEL MAHRONIC,¹
VIRAJ MANWADKAR ^{1,12,13} MICHAEL N. MARTINEZ ^{1,14} ALEXANDRA MASEGIAN ^{1,15}
OWEN S. MATTHEWS ACUÑA ^{1,16} KAIYA MERZ ¹ YUE PAN ^{1,17} JORGE A. SANCHEZ ¹ ISAAC SIERRA ¹
DANIEL J. KAVIN STEIN ¹ EZRA SUKAY ^{1,18} MARCOS TAMARGO-ARIZMENDI ¹ KIYAN TAVANGAR ^{1,15}
RUOYANG TU ^{1,19} GRACE WAGNER ¹ ERIK A. ZABOROWSKI ^{1,20,21} AND YUNCHONG ZHANG ^{1,3}

(COOL-LAMPS COLLABORATION)

¹*Department of Astronomy and Astrophysics, University of Chicago, 5640 S. Ellis Ave, Chicago, IL 60637, USA*

²*Kavli Institute for Cosmological Physics, University of Chicago, 5640 S. Ellis Ave, Chicago, IL 60637, USA*

³*Department of Physics and Astronomy, University of Pittsburgh, 3941 O'Hara St, Pittsburgh, PA 15260, USA*

⁴*Pittsburgh Particle Physics Astrophysics and Cosmology Center, University of Pittsburgh, 3941 O'Hara St, Pittsburgh, PA 15260, USA*

⁵*Department of Astronomy, University of Michigan, 1085 S. University Ave, Ann Arbor, MI 48109, USA*

⁶*Department of Astronomy, University of Massachusetts Amherst, 710 N. Pleasant St, Amherst, MA 01003, USA*

⁷*Institute of Theoretical Astrophysics, University of Oslo, P.O. Box 1029, Blindern, NO-0315 Oslo, Norway*

⁸*Department of Astronomy and Astrophysics, University of California, Santa Cruz, CA 95064, USA*

⁹*Gravitation & Astroparticle Physics, University of Amsterdam, Science Park 904, 1098 XH Amsterdam, Netherlands*

¹⁰*Department of Astronomy, University of Michigan, 1085 S. University Ave, Ann Arbor, MI, 48109, USA*

¹¹*Department of Physics and Astronomy, Stony Brook University, 100 Nicolls Rd, Stony Brook, NY 11794, USA*

¹²*Department of Physics, Stanford University, 382 Via Pueblo, Stanford, CA 94305, USA*

¹³*Kavli Institute for Particle Astrophysics and Cosmology, Stanford University, 382 Via Pueblo, Stanford, CA 94305, USA*

¹⁴*Department of Physics, University of Wisconsin, Madison, 1150 University Ave, Madison, WI 53706, USA*

¹⁵*Department of Astronomy, Columbia University, 538 W. 120th St, New York, NY 10027, USA*

¹⁶*Department of Astronomy, University of Wisconsin—Madison, 475 N. Charter St, Madison, WI 53706, USA*

¹⁷*Department of Astrophysical Sciences, Princeton University, 4 Ivy Ln, Princeton, NJ 08544, USA*

¹⁸*Department of Physics and Astronomy, Johns Hopkins University, 3400 N. Charles St, Baltimore, MD 21218, USA*

¹⁹*Department of Anthropology, Yale University, 10 Schem St, New Haven, CT 06520, USA*

²⁰*Department of Physics, The Ohio State University, 191 W. Woodruff Ave, Columbus, OH 43210, USA*

²¹*Center for Cosmology and Astro-Particle Physics, The Ohio State University, 191 W. Woodruff Ave, Columbus, OH 43210, USA*